NASA/TM—2005-213827

Prediction of Turbulence-Generated Noise in Unheated Jets

Part 1: JeNo Technical Manual (Version 1.0)

Abbas Khavaran
QSS Group, Inc., Cleveland, Ohio

James Bridges and Nicholas Georgiadis
Glenn Research Center, Cleveland, Ohio

July 2005

The NASA STI Program Office . . . in Profile

Since its founding, NASA has been dedicated to the advancement of aeronautics and space science. The NASA Scientific and Technical Information (STI) Program Office plays a key part in helping NASA maintain this important role.

The NASA STI Program Office is operated by Langley Research Center, the Lead Center for NASA's scientific and technical information. The NASA STI Program Office provides access to the NASA STI Database, the largest collection of aeronautical and space science STI in the world. The Program Office is also NASA's institutional mechanism for disseminating the results of its research and development activities. These results are published by NASA in the NASA STI Report Series, which includes the following report types:

- TECHNICAL PUBLICATION. Reports of completed research or a major significant phase of research that present the results of NASA programs and include extensive data or theoretical analysis. Includes compilations of significant scientific and technical data and information deemed to be of continuing reference value. NASA's counterpart of peer-reviewed formal professional papers but has less stringent limitations on manuscript length and extent of graphic presentations.
- TECHNICAL MEMORANDUM. Scientific and technical findings that are preliminary or of specialized interest, e.g., quick release reports, working papers, and bibliographies that contain minimal annotation. Does not contain extensive analysis.
- CONTRACTOR REPORT. Scientific and technical findings by NASA-sponsored contractors and grantees.
- CONFERENCE PUBLICATION. Collected papers from scientific and technical conferences, symposia, seminars, or other meetings sponsored or cosponsored by NASA.
- SPECIAL PUBLICATION. Scientific, technical, or historical information from NASA programs, projects, and missions, often concerned with subjects having substantial public interest.
- TECHNICAL TRANSLATION. English-language translations of foreign scientific and technical material pertinent to NASA's mission.

Specialized services that complement the STI Program Office's diverse offerings include creating custom thesauri, building customized databases, organizing and publishing research results . . . even providing videos.

For more information about the NASA STI Program Office, see the following:

- Access the NASA STI Program Home Page at ***http://www.sti.nasa.gov***
- E-mail your question via the Internet to help@sti.nasa.gov
- Fax your question to the NASA Access Help Desk at 301–621–0134
- Telephone the NASA Access Help Desk at 301–621–0390
- Write to:
  NASA Access Help Desk
  NASA Center for AeroSpace Information
  7121 Standard Drive
  Hanover, MD 21076

NASA/TM—2005-213827

Prediction of Turbulence-Generated Noise in Unheated Jets

Part 1: JeNo Technical Manual (Version 1.0)

Abbas Khavaran
QSS Group, Inc., Cleveland, Ohio

James Bridges and Nicholas Georgiadis
Glenn Research Center, Cleveland, Ohio

National Aeronautics and
Space Administration

Glenn Research Center

July 2005

Available from

NASA Center for Aerospace Information
7121 Standard Drive
Hanover, MD 21076

National Technical Information Service
5285 Port Royal Road
Springfield, VA 22100

Available electronically at http://gltrs.grc.nasa.gov

Contents

1. Nomenclature 1

2. Introduction 3

  2.1. Jet Noise Source Physics from Observations 3
  2.2. Outline of JeNo Theoretical Development 4
  2.3. Outline of Document 4

3. The Governing Equations 5

  3.1. Green's Function 6
  3.2. Multi-Pole Sources 8

4. Source Model 10

5. Spectrum Function 12

6. Numerical Evaluation of the Green's Function 12

7. Acoustic Results 13

8. Hot Jets 14

9. Assumptions and Future Work 15

10. Appendix A.—Numerical Solution to Compressible Rayleigh Equation 17

11. Appendix B.—Doppler Factor Singularity 19

12. Appendix C.—Far-Field Spectral Density 21

13. Appendix D.—Phase Variation of the Green's Function 23

14. Appendix E.—Space-Time Correlation Models 25

15. Appendix F.—Non-Compactness Factor 27

16. References 29

17. Figures 30

Prediction of Turbulence-Generated Noise in Unheated Jets
Part 1: JeNo Technical Manual (Version 1.0)

Abbas Khavaran
QSS Group, Inc.
Cleveland, Ohio 44135

James Bridges and Nicholas Georgiadis
National Aeronautics and Space Administration
Glenn Research Center
Cleveland, Ohio 44135

Abstract

The model-based approach, used by the JeNo code to predict jet noise spectral directivity, is described. A linearized form of Lilley's equation governs the non-causal Green's function of interest, with the non-linear terms on the right hand side identified as the source. A Reynolds-averaged Navier-Stokes (RANS) solution yields the required mean flow for the solution of the propagation Green's function in a *locally parallel* flow. The RANS solution also produces time- and length-scales needed to model the non-compact source, the turbulent velocity correlation tensor, with exponential temporal and spatial functions. It is shown that while an exact non-causal Green's function accurately predicts the observed shift in the location of the spectrum peak with angle as well as the angularity of sound at low to moderate Mach numbers, the polar directivity of radiated sound is not entirely captured by this Green's function at high subsonic and supersonic acoustic Mach numbers. Results presented for unheated jets in the Mach number range of 0.51 to 1.8 suggest that near the peak radiation angle of high-speed jets, a different source/Green's function convolution integral may be required in order to capture the peak observed directivity of jet noise. A sample Mach 0.90 heated jet is also discussed that highlights the requirements for a comprehensive jet noise prediction model.

1. Nomenclature

x_i	Cartesian coordinate components; i = 1 denotes axial direction
y_i	Cartesian coordinate components
ξ_i	displacement vector components
ξ	displacement vector magnitude
t	time
ρ	density
p	pressure
T	temperature
T_r	temperature ratio, plenum to ambient
v_i	velocity component
u_i	fluctuating velocity component
c	speed of sound, $=\sqrt{\gamma \Re T}$
U	axial mean velocity
U_J	velocity at jet exit
D_J	jet diameter
D	Green's function directivity function.

L	Pridmore-Brown operator
Π	reduced pressure $\prod \equiv (1/\gamma)\ 1\text{n}(p/p_o)$
δ_{ij}	Kronecker delta
δ	delta function
γ	specific heat ratio
π'	dependent variable for pressure
ζ_i	source component, (eq. 3)
f	frequency
f_m	m^{th} mode of solution to second-order compressible Rayleigh operator
h	enthalpy
r	Cartesian coordinate, radial component
R	spherical coordinate component, radius; distance to observer
θ	spherical coordinate component, polar angle
φ	spherical coordinate component, azimuthal angle
ω	frequency, $2\pi f$
M	Mach number
St	Strouhal number, $\omega D_J/(2\pi U_J)$
He	Helmholtz number, $\omega D_J/(2\pi c_\infty)$
k	acoustic wavenumber
τ	time delay coordinate
τ_o	turbulent timescale
ℓ	turbulent lengthscale
κ	turbulent kinetic energy
ε	turbulent dissipation rate
I_{ijkl}	two-point, fourth-order space-time correlation of velocity
R_{ij}	two-point, second-order, spatial correlation of velocity
h	temporal correlation function
H	Fourier transform of temporal correlation function h
N	non-compactness factor
c_ℓ	calibration constant associated with lengthscale
c_τ	calibration constant associated with timescale
A_m	calibration constant associated with conversion of turbulent kinetic energy to acoustic energy
α	calibration constant to remove singularity of Doppler factor
F	master spectrum, spectral function at $\theta = 90°$
$\mathbb{G}$, $\hat{\mathbb{G}}$	Green's functions
$()_c$	() convecting
$()_\infty$	() at far-field
$()'$	fluctuating portion of ()
$()^s$	() evaluated at source location
$()_t$	() evaluated at transverse location
$[]_m$	[] in moving frame
$\overline{()}$	time average of ()

2. Introduction

There is an ever-increasing demand on the aeroacoustics community to achieve new levels of accuracy in noise prediction in order to meet the stringent regulations set for aircraft noise reduction. Jet noise is of particular interest because of its dominant contribution to the noise radiated from aircraft engines operating at high thrust conditions during takeoff. As part of an ongoing research program at the NASA Glenn Research Center, the JeNo code is being developed to provide the state-of-the-art in jet noise source modeling and propagation. Since jet mixing-noise is broadband, with frequencies that cover a full three-octave range, a successful source model needs to bring in enough physics to predict a reasonably acceptable spectral density at various operating conditions.

This document, *Part 1: JeNo Technical Manual,* details the theoretical development of JeNo version 1.0. It discusses the jet physics being captured by the code, the mathematical derivation of the equations, the assumptions and models which are captured in the computer code. This document is for the user who wishes to understand the limitations of JeNo with either an eye to understanding the output or to improving its shortcomings. A separate document, *Part 2: JeNo Users Manual*, covers the operation of the code from the computer user's point of view, including code architecture, input and output formats, and examples.

2.1 Jet Noise Source Physics from Observations

Experimental observations of jet noise spectra and directivity for a wide range of shock-free operating conditions show that a bi-modal description best fits a typical spectrum. This has prompted many to propose a two-source generation mechanism. In the broadside angles, jet noise is usually attributed to small-scale turbulence. Prediction schemes such as MGBK (ref. 1) or Tam and Auriault (ref. 2) scale the sound spectral density to 7/2 power of turbulence kinetic energy and use a Reynolds-averaged Navier-Stokes (RANS) solution to estimate the source strength and its spectral shape. The general shape of the spectrum and its roll-off at the high- and low ends of its frequency range depends on the proposed source model as well as the accuracy of the propagation filter, i.e., the Green's Function (GF). The non-causal GF solution of interest may be obtained from the inhomogeneous Lilley's equation or directly from linearized Euler equations using numerical methods or some form of analytical approximation. This is the source being addressed in version 1.0 of the JeNo code.

At aft angles, the non-causal GF solution predicts a strong increase in sound, but not as strong as observed in jet experiments at supersonic Mach numbers. A second mechanism for sound generation is commonly proposed, being attributed to the large-scale turbulent structures, which are considered as a superposition of instability modes of the mean flow. It has been shown that when the base flow is properly represented as a non-parallel jet, these waves grow in amplitude and then decay farther downstream. They become increasingly more efficient with jet speed, and at small angles from the downstream axis. While this mechanism is often called a second source, a recent study (ref. 3) describes instability waves as a second 'conduit' that helps carry the sound from the source region to the far field rather than acting as a separate source. In this view, a two-component spectrum may be thought of as the contributions from two completely different Green's functions acting on the same source. This second 'conduit', expressed by a causal GF, is not addressed in version 1.0 of the JeNo code.

To summarize, version 1.0 of JeNo is applicable to cold, round jets of subsonic velocity. It correctly predicts sound for all angles at such conditions. It does not correctly predict hot jets, jets of strong asymmetry, or jets with supersonic (relative to ambient speed of sound) exit velocities.

2.2 Outline of JeNo Theoretical Development

The non-causal GF described in the present paper is derived from Lilley's equation. A good approximation to the base flow that is useful for jets and adopted here is a unidirectional transversely sheared mean flow or a locally parallel flow. From a practical point of view, this flow provides added numerical efficiency with minimal degradation in accuracy. Deviations from a true spreading jet are usually limited to a small angle range close to the jet axis and near the zone of silence where the contribution from a causal GF is likely to dominate.

Upon linearizing the Navier-Stokes equations about the base flow (for an ideal gas), the nonlinear terms are moved to the right-hand side to obtain the inhomogeneous Pridmore-Brown equation (ref. 4). The right-hand side terms, all second-order in fluctuating variables, are now identified as the *equivalent* sources. Fluid viscosity and heat conduction are considered to be relatively unimportant in noise generation and are neglected compared to other source terms. Two of the three remaining sources are quadrupole in nature and are referred to as the self- and shear-noise source terms. The third source has a dipole character and is associated with temperature fluctuations.

Solving the equations for the far-field observer then consists of two tasks: modeling the source terms and finding the solution to the Pridmore-Brown equation. The first is done by assuming functional forms for the different terms and applying proper scaling factors from turbulence models, usually obtained from CFD. The second is done by constructing a Green's function (GF) which satisfies the propagation equation for a point source embedded in the flow, which is also usually known from CFD. This GF then acts as a filter to describe the relationship between the sources and the observer.

A model-based approach usually relies on averaged equations of motion. Statistical properties of noise sources, as described by a two-point space-time correlation, are entirely modeled. A physics-based modeling of sources can be improved as our understanding of the underlying generation mechanism and turbulence details advances. The current source models represent current understanding of the turbulence correlation tensor and will undoubtedly be improved upon in future versions. It is important that the source model be kept independent of propagation effects so that improvements in the source model not be masked by improper fixes to the propagation portion of the code.

In addition to the source description, the propagation filter needs to be accurate enough to capture refraction and shielding of sound for a wide range of frequencies, angles, and operating conditions. A review of some commonly used high-frequency asymptotic forms of the GF following the usual WKB methods and comparison with the numerical solution (ref. 5) demonstrates that these solutions generally remain accurate down to a Strouhal number of 0.5. However, the extension of the WKB solution to the more general jets with multiple turning points presents additional challenges and may require a numerical calculation of the near-field solution in order to satisfy the matching conditions. Indeed, the initial version of JeNo differs from its ancestor, the MGBK code, primarily in its use of the more rigorous GF solution, obtained using adjoint methods.

2.3 Outline of Document

The objective of this paper is to present the details of the source as well as the GF in a model-based prediction approach. The analytical solution to the intensity calculations using an exact GF is given in section 3. Section 4 shows the modeling of the two-point velocity correlations using an exponential form to describe both spatial and temporal functions. The general features of the 90° spectrum are addressed in section 5. A parametric study of the GF using a RANS-based mean flow is discussed in section 6. In particular, it is demonstrated that the mean flow could have an amplifying effect on radiated sound at certain observer angles and at certain source locations. More importantly, it is argued that regardless of the source definition used in the convolution integral, a non-causal GF, due to its sizable zone of silence, is incapable of capturing the observed directivity of high-speed jets at their peak radiation angle. Sample noise predictions are presented in section 7 for a number of unheated jets in the Mach number range 0.51

through 1.80, and compared with data recently collected at the Small Hot Jet Acoustic Rig (SHJAR) at the NASA Glenn Research Center. Section 8 studies a Mach 0.90 heated jet at a stagnation temperature ratio of 3.14. The hot jet exercise considers two important scaling rules related to the GF, and proposes a number of turbulence-related issues that need to be examined carefully prior to the addition of a heat-related source. A summary of assumptions adopted in the present analysis will be reviewed in section 9. Requirements for developing a comprehensive physics-based jet noise prediction algorithm will also be discussed.

3. The Governing Equations

Lilley's third-order wave equation (ref. 6) may be linearized about a unidirectional transversely sheared mean flow

$$p_o = \text{constant}, \quad U_i = \delta_{i1} U(x_2, x_3), \quad T_o = T_o(x_2, x_3).$$

and rearranged to a form commonly referred to as the Pridmore-Brown (ref. 4) equation

$$L\Pi \equiv \frac{D}{Dt}\left(\frac{D^2\Pi}{Dt^2} - \frac{\partial}{\partial x_j}(c^2 \frac{\partial \Pi}{\partial x_j})\right) + 2c^2 \frac{\partial U}{\partial x_j}\frac{\partial^2 \Pi}{\partial x_1 \partial x_j} = \Gamma \quad . \tag{1}$$

Here Γ is the source, $\vec{x} \equiv (x_1, x_2, x_3)$ are the Cartesian coordinates and x_1 is in the stream-wise direction, p is pressure and p_o is the mean pressure, (i.e., $p \equiv p_o + p'$), $\Pi \equiv (1/\gamma)\ 1\text{n}(p/p_o)$, $c^2 = \gamma \Re T_o$ is the mean sound speed, t is time, and the convective derivative operator is

$$\frac{D}{Dt} \equiv \frac{\partial}{\partial t} + U\frac{\partial}{\partial x_1}.$$

When pressure fluctuations p' are small relative to mean pressure p_o, the dependent variable is approximated as $\Pi \cong p'/(\gamma p_o)$. Goldstein (refs. 7 and 8) carried out a second-order expansion of equation (1) and introduced a new dependent variable $\pi' \equiv \Pi + \Pi^2/2$ to show that

$$L\pi' = \frac{D}{Dt}\frac{\partial \zeta_i}{\partial x_i} - 2\frac{\partial U}{\partial x_i}\frac{\partial \zeta_i}{\partial x_1} \tag{2}$$

and

$$\zeta_i \equiv \frac{\partial(u_i u_j)}{\partial x_j} + (c^2)'\frac{\partial \Pi}{\partial x_i}, \tag{3}$$

where $u_i \equiv v_i - \delta_{i1}U$ denotes the velocity fluctuations. The source term (3) may be approximated as $\zeta_i \cong \partial(u_i u_j)/\partial x_j$ once fluctuations in sound speed $(c^2)' = \gamma \Re (T - T_o)$ are neglected (a valid approximation when jet is isothermal). With the dependent variable approximated as $\pi' \cong \Pi$ (see ref. 9) for the equation governing Π^2), equation (2) becomes

$$L\Pi \cong \frac{D}{Dt}\frac{\partial^2 (u_i u_j)}{\partial x_i \partial x_j} - 2\frac{\partial U}{\partial x_i}\frac{\partial^2 (u_i u_j)}{\partial x_1 \partial x_j}, \quad \Pi \cong \frac{p'}{\gamma p_o} \tag{4}$$

An alternate definition for the dependent variable is $\pi' \equiv (p/p_o)^{1/\gamma} - 1$. As shown in (ref. 7), with this new parameter, equation (2) becomes an exact rearrangement of the Euler equations once the source is defined as

$$\zeta_i \equiv \frac{\partial}{\partial x_j}(1+\pi')u_i u_j + (\gamma - 1)\mathrm{h}'\frac{\partial \pi'}{\partial x_i}$$

This latter source reduces to that defined in equation (3) when enthalpy fluctuation h' is written as $\mathrm{h}' = (\gamma - 1)(c^2)'$ and if π' is considered small relative to unity.

The *equivalent* sources of sound in a Lilley-type analogy are second-order in fluctuating variables. It has been pointed out repeatedly in the literature that the main difference between Lighthill and Lilley's formulation of the acoustic analogy is a separation of the propagation effect from the source in the latter formulation, which presumably places less demand on the details of the source modeling. The GF calculations described in section 6 clearly show the significance of the Lilley operator in isolating the propagation effect.

There have been numerous efforts in the past half-century to experimentally measure the actual sources of sound in a turbulent flow. Measurement techniques such as phased-array can measure the relative source strength and its frequency content at various regions in a jet. Particle Image Velocimetry (PIV) methods have been instrumental in turbulence and correlation measurements. When combined, the two techniques may establish a link between the turbulent flow and the far-field sound it produced. This rather laborious and cumbersome process is used in concept studies and parameter selection.

The analysis presented in this paper is based on equation (4). The 2nd order terms on the right side of the above equation are referred to as self- and shear-noise source terms, respectively.

3.1 Green's Function

A stationary point source with frequency ω and location $\vec{x}^s$ (superscript s denotes a source location) is considered in defining the GF

$$L(\mathbb{G}e^{-i\omega t}) = c_\infty^2 e^{-i\omega t}\delta(\vec{x} - \vec{x}^s) \tag{5}$$

Using an adjoint method (ref. 10), the far-field GF is given as

$$\mathbb{G}(\vec{x}, \vec{x}^s, \omega) = \frac{1}{4\pi\omega R} e^{ik(R - x_1^s \cos\theta)} \sum_{m=0}^{\infty} f_m(r^s, k, \theta)\cos m(\varphi - \varphi^s) \quad , \tag{6}$$

where (R, θ, φ) are the observer spherical coordinates, with radius R measured from the jet exit centerline, polar angle θ measured from the stream-wise jet axis, and azimuthal angle φ is measured in a span-wise plane. Wave number is defined as $k = \omega/c_\infty$ and $r \equiv R \sin\theta$. Function $f_m(r, k, \theta)$ is a solution to the second-order compressible Rayleigh operator subject to appropriate matching conditions at the jet boundary (app. A). The linear operator L also supports instability waves, which for a jet are the well-known Kelvin-Helmholtz instabilities. Reference 11 argues that these waves are suppressed if the governing equations are solved in a frequency domain and if a time-harmonic response is assumed.

For a source type $D/Dt[c_\infty^2 e^{-i\omega t}\delta(\vec{x}-\vec{x}^s)]$, representative of the self-noise term in equation (4), the GF is denoted as $\hat{\mathbb{G}}$, and is related to $\mathbb{G}$ as $\hat{\mathbb{G}} = -(i\omega + U\partial/\partial x_1^s)\mathbb{G}$, which upon using equation (6) becomes

$$\hat{\mathbb{G}} = -i\omega(1-M^s\cos\theta)\mathbb{G} \tag{7}$$

Here $M^s \equiv U(r^s)/c_\infty$ is the acoustic Mach number at the source location.

The GF of interest in jet noise is associated with a moving singularity with source frequency ω^s and convection velocity $\hat{i}\,U_c$. For self-noise we write

$$L(Ge^{-i\omega t}) = \frac{D}{Dt}\{c_\infty^2 e^{-i\omega^s t}\delta(x_1 - U_c t)\delta(\vec{x}_t - \vec{x}_t^s)\} \tag{8}$$

Subscript t denotes a transverse location. The above GF is derived from equation (7) and a convolution integral as

$$G(\vec{x},\vec{x}^s,\omega)e^{-i\omega t} = \frac{1}{2\pi}\int_\omega d\omega \int_{\vec{y}}\int_\tau \hat{\mathbb{G}}(\vec{x},\vec{y},\omega)e^{-i\omega t}e^{-i(\omega^s-\omega)\tau}\delta(\vec{y}_t - \vec{x}_t^s)\delta(y_1 - U_c\tau)\,d\tau d\vec{y} \tag{9}$$

Integrating with respect to τ and $\vec{y}_t$ yields

$$G(\vec{x},\vec{x}^s,\omega)e^{-i\omega t} = \frac{1}{2\pi U_c}\int_\omega d\omega \int_{y_1}\hat{\mathbb{G}}(\vec{x};\vec{x}_t^s,y_1;\omega)e^{-i\omega t}e^{-i(\omega^s-\omega)y_1/U_c}dy_1 \tag{10}$$

Using $\hat{\mathbb{G}}$ from equations (7) and (6) into equation (10) and invoking the parallel flow assumption; the integration with respect to y_1 yields a delta function

$$\int_{y_1} e^{-iky_1\cos\theta}e^{-i(\omega^s-\omega)y_1/U_c}dy_1 = 2\pi\delta[-\frac{\omega}{U_c}(1-M_c\cos\theta)+\frac{\omega^s}{U_c}], \tag{11}$$

Where $M_c = U_c/c_\infty$ is the convective Mach number.

Placing equation (11) in equation (10), the integration with respect to ω is readily carried out

$$G(\vec{x},\vec{x}^s,\omega)e^{-i\omega t} = \frac{-i}{4\pi R}\frac{(1-M^s\cos\theta)}{(1-M_c\cos\theta)}e^{\frac{-i\omega^s t}{1-M_c\cos\theta}}.e^{\frac{i\omega^s/c_\infty}{1-M_c\cos\theta}R}\sum_m f_m(r^s,\frac{\omega^s/c_\infty}{1-M_c\cos\theta},\theta)\cos m(\varphi-\varphi^s) \tag{12}$$

Upon relating source and observer frequencies through the Doppler factor

$$\omega = \frac{\omega^s}{1-M_c\cos\theta}, \tag{13}$$

the GF to equation (8) becomes

$$G(\vec{x},\vec{x}^s,\omega)=\frac{-i}{4\pi R}\frac{(1-M^s\cos\theta)}{(1-M_c\cos\theta)}e^{ikR}\sum_m f_m(r^s,k,\theta)\cos m(\varphi-\varphi^s) \tag{14}$$

When the source is moving, the Doppler factor becomes singular in the direction $\theta = \cos^{-1}(1/M_c)$. By considering the source as non-compact (app. B), a modified Doppler factor is defined that should be used near this singularity.

Equation (14) indicates that the adjoint equation should be solved at the observer frequency even though the source is moving. In addition, it illustrates that for a convecting type source, the dependence of the GF on the axial source location is purely implicit, i.e., through the flow definition at the jet slice. Once the adjoint equation is solved for given values of observer angle θ, Strouhal number St, and mode number m, function f_m should be known at any arbitrary source locations r^s on the jet slice. Strouhal number is defined using exit diameter and jet exit velocity $St = \omega D/(2\pi U_J)$.

3.2 Multi-Pole Sources

The far-field spectral density may be expressed as the integration of the sound spectral density per unit volume of turbulence with respect to the source volume $\vec{y}$ (app. C).

$$\overline{p^2}(\vec{x},\vec{y},\omega)=\int_{\vec{\xi}}\int_{-\infty}^{+\infty}G^*(\vec{x},\vec{y}-\vec{\xi}/2,\omega)G(\vec{x},\vec{y}+\vec{\xi}/2,\omega)R(\vec{y},\vec{\xi},\tau)e^{i\omega\tau}d\tau d\vec{\xi} \tag{15}$$

Here $R(\vec{y},\vec{\xi},\tau)$ denotes a two-point fourth-order space-time correlation between source points $\vec{y}_1=\vec{y}-\vec{\xi}/2$ and $\vec{y}_2=\vec{y}+\vec{\xi}/2$ separated by time τ and space $\vec{\xi}$. In a compact eddy approximation, the variation of the GF within the source region is usually neglected and the product GG^* is approximated as the square of the magnitude of the GF at the center of the correlation $\vec{y}$, and taken out of the above integral. The phase variation in the GF, however, could become a factor at high frequency when the correlation length scale exceeds the acoustic wavelength. The complex function f_m appearing in the series summation of equation (14) contains the phase information of the GF. To simplify the analysis, a form of the phase factor applicable in the high-frequency limit is used here (app. D)

$$\overline{p^2}(\vec{x},\vec{y},\omega)=\left|G(\vec{x},\vec{y},\omega)\right|^2\int_{\vec{\xi}}\int_{-\infty}^{+\infty}e^{-i\vec{k}.\vec{\xi}}R(\vec{y},\vec{\xi},\tau)e^{i\omega\tau}d\tau d\vec{\xi} \tag{16}$$

The above double integral, referred to as the wave-number frequency spectrum, may be expressed either in a fixed or a moving frame. In a convecting frame, $\vec{\xi}_m=\vec{\xi}-\hat{i}\,U_c\tau$, and $R(\vec{y},\vec{\xi},\tau)=R_m(\vec{y},\vec{\xi}_m,\tau)$, hence

$$\int_{-\infty}^{+\infty}e^{i\omega\tau}d\tau\int_{\vec{\xi}}R(\vec{y},\vec{\xi},\tau)\,e^{-i\vec{k}.\vec{\xi}}d\vec{\xi}\equiv\int_{-\infty}^{+\infty}e^{i\omega^s\tau}d\tau\int_{\vec{\xi}_m}R_m(\vec{y},\vec{\xi}_m,\tau)\,e^{-i\vec{k}.\vec{\xi}_m}d\vec{\xi}_m \tag{17}$$

A spectral coefficient for a two-point fourth-order correlation of stress component $u_i u_j$ at points $\vec{y}$ and $\vec{y}'$ is defined as (prime designates separation in space and time)

$$I_{ijkl}(\vec{y},\omega) \equiv \int_{\vec{\xi}} \int_{-\infty}^{+\infty} \overline{(u_i u_j)(u_k' u_l')}\, e^{-i\vec{k}.\vec{\xi}} e^{i\omega\tau} d\tau d\vec{\xi} \tag{18a}$$

Upon recognizing that $-\vec{k}.\vec{\xi} + \omega\tau = -\vec{k}.\vec{\xi}_m + \omega^s \tau$, the above integral is written in a moving frame

$$I_{ijkl}(\vec{y},\omega^s) \equiv \int_{\vec{\xi}_m} \int_{-\infty}^{+\infty} [\overline{(u_i u_j)(u_k' u_l')}\,]_m e^{-i\vec{k}.\vec{\xi}_m} e^{i\omega^s\tau} d\tau d\vec{\xi}_m \tag{18b}$$

Subscript m under the square bracket in equation (18b) denotes a moving frame two-point correlation, which is related to the nozzle-fixed correlation by an exchange of $\zeta_1 - U_c\tau$ in the latter with $(\zeta_1)_m$. The over-bar points to a time-averaged quantity. Presence of double derivatives operating on the source terms of equation (4) indicates that the appropriate GF should ultimately be calculated for a singularity type

$$\frac{D}{Dt}\{c_\infty^2 \frac{\partial^2}{\partial x_i \partial x_j} e^{-i\omega^s t} \delta(x_1 - U_c t)\delta(\vec{x}_t - \vec{x}_t^s) Q_{ij}\} \tag{19}$$

The analysis may be carried out as described in the convolution integral leading to equation (9). However, the source spatial derivatives are now moved to the GF prior to $\vec{y}$ integration. For example, an application of $\partial^2 / \partial y_1 \partial y_1$ to $\hat{\mathbb{G}}(\vec{x},\vec{y};\omega)$ in the integrand of equation (9) generates $(-ik\cos\theta)^2$ as seen from equation (6). Subsequently, $(k\cos\theta)^4$ multiplies sound intensity due to source correlation $\overline{(u_1 u_1)(u_1' u_1')}$. A derivative of $\hat{\mathbb{G}}$ with respect to the span-wise source coordinates y_2 or y_3, acts on $f_m(r^s,k,\theta)\cos m(\varphi - \varphi^s)$. The algebra is quite lengthy but relatively straightforward. It may be shown that to the first order of approximation, quadrupoles of self noise, once integrated azimuthally for a ring volume within an axisymmetric jet, relate to the axial component I_{1111}. For an isotropic turbulence the result simplifies to

$$(1 - M^s \cos\theta)^4 (\rho^s)^2 k^4 I_{1111} \tag{20}$$

This, in view of equation (14), leads to the following expression for the sound spectral density per unit ring volume at radius r^s

$$\overline{p_{self}^2}(\vec{x},\vec{y},\omega) \cong \frac{1}{(4\pi R)^2} \frac{(1 - M^s\cos\theta)^6}{(1 - M_c\cos\theta)^2} \left(\frac{\rho^s}{\rho_\infty}\right)^2 (\rho_\infty^2 I_{1111}) k^4 \sum_m \left| f_m(r^s,k,\theta)\right|^2 \tag{21}$$

The above result is integrated over jet volume elements that radiate directly to the far field. Noise from sources internal to the jet requires special treatment due to reflection from solid boundaries. An approximate high-frequency solution for sound emission due to internal mixing is given in reference 12.

It will be shown in section 7 that equation (14) scales like $\rho^{1/2}$ with jet density, hence sound spectral density in equation (21) scales with ρ^3.

4. Source Model

The axial correlation coefficient needed in equation (21) is obtained from equation (18) when all indices are set equal to one. Using the usual quasi-normal approximation for the joint probability distribution of turbulence (refs. 13 and 14), a fourth-order correlation is written as a product of second-order tensors.

$$\overline{u_i u_j u_k^{'} u_\ell^{'}} = (\overline{u_i u_j})(\overline{u_k^{'} u_\ell^{'}}) + (\overline{u_i u_k^{'}})(\overline{u_j u_\ell^{'}}) + (\overline{u_i u_\ell^{'}})(\overline{u_j u_k^{'}}) \tag{22a}$$

A nozzle-fixed second-order correlation is written as

$$\overline{u_i u_j^{'}}(\vec{\xi}, \tau) = R_{ij}(\vec{\xi} - \hat{i}\, U_c \tau) h(\tau) \tag{22b}$$

Appropriate modeling of a two-point velocity correlation is a crucial step in a physics-based prediction approach. As shown in reference 1 the best representation of the experimental measurements (refs. 15, 16, and 17) are obtained when exponential functions are selected to represent both spatial and temporal dependencies of the correlation (also see app. E)

$$f(\xi_m) \equiv e^{-\pi \xi_m / \ell}, \quad h(\tau) \equiv e^{-|\tau / \tau_o|} \tag{23}$$

In equation (23), $\xi_m \equiv |\vec{\xi}_m|$ is measured in a moving frame, and is equivalent to $[(\xi_1 - U_c \tau)^2 + \xi_2^2 + \xi_3^2]^{1/2}$ if used in a fixed frame, and f is the scalar function that appears in the isotropic from of Rij.

In an isotropic turbulence, various components of a two-point correlation are obtained from placing equation (23) in Batchelor's isotropic turbulence model ref. 14)–for example, the fixed-frame axial component of the correlation is written in the following non-separable form

$$\overline{u_1 u_1^{'}}(\vec{\xi}, \tau) = \overline{u_1^2}\,[1 - \frac{\pi}{2\xi\ell}(\xi_2^2 + \xi_3^2)]\, e^{-\pi \xi / \ell} e^{-|\tau / \tau_o|}, \quad \xi = [(\xi_1 - U_c \tau)^2 + \xi_2^2 + \xi_3^2]^{1/2}$$

Parameters ℓ and τo denote the length- and time-scales of the correlation

$$\ell \equiv c_\ell \kappa^{3/2} / \varepsilon, \quad \tau_o \equiv c_\tau \kappa / \varepsilon \tag{24}$$

Turbulence kinetic energy κ and its dissipation rate ε are usually provided through a RANS type solution and (c_ℓ, c_τ) represent a pair of calibration constants.

Using a quasi-normal approximation, and substituting equation (22b) in equation (18b) shows that

$$I_{1111}(\vec{y}, \omega^s) = 2H(\omega^s) \int_{\vec{\xi}_m} R_{11}^2(\vec{\xi}_m) e^{-i\vec{k} \cdot \vec{\xi}_m} d\vec{\xi}_m, \tag{25}$$

$$H(\omega^s) \equiv \int_{-\infty}^{+\infty} h^2(\tau) e^{i\omega^s \tau} d\tau \tag{26}$$

Upon representing $R_{11}(\vec{\xi}_m)$ according to the homogeneous isotropic model of Batchelor (ref. 14) with f as defined in equation (23), it is shown (ref. 1) that

$$I_{1111}(\vec{y},\omega^s) = \frac{4}{5\pi^2}(\overline{u_1^2})^2 \ell^3 H(\omega^s) N(k\ell) \tag{27}$$

Here $N(k\ell)$ denotes a non-compactness factor (app. F), which appears in the analysis due to the phase variation of the GF. As was discussed in reference 1, $N(k\ell)$ remains equal to 1.0 when $0 \le k\ell < 2\pi$, and decays rapidly as the eddy length-scale exceeds the wave-length of acoustic disturbances (i.e., $k\ell > 2\pi$).

Carrying out the integration in equation (26) in conjunction with equation (23) results in

$$H(\omega^s) = \frac{\tau_o}{1+(\omega^s \tau_o / 2)^2} \tag{28}$$

Upon using equations (24) and (28) in equation (27) and replacing $\overline{u_1^2}$ with $2\kappa/3$ gives

$$I_{1111}(\vec{y},\omega^s) = \frac{16}{45\pi^2}(\frac{c_\ell}{c_\tau})^3 \kappa^{7/2} \frac{\tau_o^4}{1+(\omega^s \tau_o / 2)^2} N(k\ell) \tag{29}$$

Equation (29) shows that at constant τ_o sound intensity scales with $\kappa^{7/2}$. A third calibration constant A_m should multiply equation (29) to account for the fraction of turbulence kinetic energy converted to sound. This factor is combined with other constants preceding $\kappa^{7/2}$

$$I_{1111}(\vec{y},\omega^s) = A_m \kappa^{7/2} \frac{\tau_o^4}{1+(\omega^s \tau_o / 2)^2} N(k\ell) \tag{30}$$

Equation (21) in conjunction with equation (30) is integrated over the jet volume (all rings within each slice) to calculate the far-field sound due to self-noise sources.

The appropriate GF for shear-noise source term is similar to equation (14), but divided by $\omega(1-M^s\cos\theta)$. Once the variations in dU/dr within the source correlation volume are neglected, the shear-noise spectral density due to a unit ring volume may be approximated as

$$\begin{aligned}\overline{p_{shear}^2}(\vec{x},\vec{y},\omega) \cong \frac{1}{(4\pi R)^2} \frac{(\frac{2dU/dr}{\omega})^2}{(1-M_c\cos\theta)^2}(\frac{7}{2}\cos^2\theta)\left(\cos^2\theta + \frac{(1-M^s\cos\theta)^2}{c^2/c_\infty^2}\right) \\ \times(\rho_\infty^2 I_{1111})k^4 \sum_m \left| f_m(r^s,k,\theta)\right|^2 .\end{aligned} \tag{31}$$

This expression remains small at and near mid angles; however it generates significant directivity away from 90° as opposed to the self-noise spectrum, which is more omni-directional.

The coupling between self- and shear-noise terms is neglected in the following predictions.

5. Spectrum Function

The spectral shape at 90°, also referred to as the master spectrum, is derived from the product $k^4 H(\omega)N(k\ell)$, as seen from equations (21) and (30). It takes the following form once turbulence correlation is modeled according to equation (23)

$$F(\omega\tau_o) \equiv \frac{(\omega\tau_o)^4}{1+(\omega\tau_o/2)^2} N(k\ell) \tag{32}$$

In the absence of factor $N(k\ell)$, function $F(\omega\tau_o)$ becomes infinite like ω^2 as $\omega \to \infty$. On the other hand, with increasing ω the phase variation in the GF becomes increasingly significant as the eddy correlation length exceeds the acoustic wavelength. The spectral function $F(\omega\tau_o)$ decays at large frequencies as ω^{-3} once factor $N(k\ell)$ is included (fig. 1). This practically amounts to limited self-cancellation of high wave-number components of noise within the correlation. Also shown in this figure is the 90° spectrum function as calculated with temporal function $h(\tau) \equiv \exp[-\sqrt{(\sigma/2)^2 + (\tau/\tau_o)^2}]$. The small constant σ would assure high-frequency decay even with factor $N(k\ell)$ selected as 1.0; however the spectrum becomes narrower. A Gaussian temporal function $\exp(-\tau^2/\tau_o^2)$ generates a relatively narrow spectral range due to its steep roll-off at high frequency and may not be a suitable model for jet noise prediction.

6. Numerical Evaluation of the Green's Function

In this section numerical calculation of the GF is presented for a range of parameters of common interest in jet noise prediction. A careful study of this non-causal GF and its association with the source location, frequency, and jet speed provides valuable insight into its contribution to a total solution.

In a *locally parallel flow*, jet profiles (i.e., mean axial velocity and temperature) as defined at each stream-wise location x_1, are utilized in solving the propagation equation (A1), subject to the boundary conditions defined in appendix A. The GF is calculated from the series summation equation (14)–and subsequently normalized and integrated azimuthally to define ring source directivity

$$D^2(\vec{x}, \vec{x}^s, \omega) \equiv \frac{(4\pi R)^2}{2\pi} \int_{-\pi}^{+\pi} \left| G(\vec{x}, \vec{x}^s, \omega) \right|^2 d\varphi^s \tag{33}$$

Both stationary and convecting type sources are considered. Source convection velocity is defined as a weighted average of local and exit velocities as supported by measurements (ref. 18)

$$U_c(r, x_1) = 0.50U(r, x_1) + 0.25U_j \tag{34}$$

Alternative expressions (ref. 19) for U_c based on local, exit, and ambient jet velocities are available and could readily be tested. When the denominator of equation (14) becomes singular, it is replaced with a modified Doppler factor (app. B).

Mean flow predictions (RANS) were generated for a Mach 0.90 unheated jet using the Wind flow solver (ref. 20) available at the NASA Glenn Research Center. Source location $\vec{y}$ is identified through the ring radius r^s and its distance from the jet exit x_1^s.

Directivity D for a stationary ring source at one diameter from jet the exit, and for selected values of St from 0.10 to 5.0 is shown in figures 2(a) through (d). It is observed that sources in the proximity of the jet centerline produce a larger directivity. The zone of silence grows noticeably in size with increasing frequency as expected. As seen in figures 2(c) and (d), the zone of silence may grow as large as 60° (relative to the jet axis) for the more energetic segments of the jet, i.e., the jet mixing layer. Figures 3(a) through (d) use the flow definition at x_1^s=7.5D to highlight the significance of the jet profile on sound refraction. It is noted that source strength should ultimately multiply the GF when calculating the actual sound spectrum.

Source convection is known to amplify the radiated sound in the mean flow direction. This is illustrated in figures 4 and 5, which should be compared with the figures 2(b) and 3(b) for similar stationary sources.

7. Acoustic Results

A total of seven unheated cases (stagnation temperature ratio of 1.0) are shown in table 1, with the aerodynamic Mach number extending from 0.51 to 1.80. All nozzles have a 2 in. exit diameter. The first two set points are subsonic–and utilize an Acoustic Reference Nozzle (ARN2). The supersonic set points use Convergent-Divergent (CD) nozzles designed to provide perfectly expanded exit conditions using a Method of Characteristic approach. The fully expanded (design) Mach numbers are 1.185, 1.40, 1.50, 1.66, and 1.80. Jet mixing noise was predicted on an arc R/D_J = 100, and compared with SHJAR data recently acquired at the NASA Glenn Research Center. Atmospheric attenuation has been removed from all measurements in order to make a lossless comparison with predictions. Although special care has been taken to test each CD nozzle at its design pressure ratio, shock-associated noise and screech-related spikes are noticeable in the measurements. RANS solutions were generated using the in-house Wind code with a standard κ–ε turbulence model. Upstream nozzle conditions were specified in terms of plenum temperature ratio T_r and the pressure ratio.

TABLE 1.—UNHEATED JETS (T_R = 1.0)

Case	Mach No.	U_J / c_∞
SP03	0.51	0.50
SP07	0.98	0.90
M1.18	1.185	1.047
M1.40	1.40	1.186
M1.50	1.50	1.245
M1.66	1.66	1.33
M1.80	1.80	1.40

TABLE 2.—HEATED JET (T_R = 3.14)

Case	Mach No.	U_J / c_∞
SP49	0.90	1.48

An additional heated (nearly sonic) case, SP49, will also be considered to highlight the shortcomings in our hot jet predictions and to suggest possible solutions.

Calibration constants c_τ, c_ℓ (see eq. 24) and A_m (see eq. 30) are determined for the best fit with respect Mach 0.51 jet. The fidelity of the solution is then examined for the range of Mach numbers. The argument of the non-compactness factor $k\ell = (2\pi St)(\ell / D_J)(U_J / c_\infty)$ would become self-similar across a wide range of Mach number when divided by the local acoustic Mach number $U(r^s)/c_\infty$, as both factors ℓ / D_J and $U_J/U(r^s)$ are now self-similar. This modified argument is deployed in noise predictions.

Figure 6 shows the spectra for a Mach 0.51 cold jet at selected inlet angles. The self-noise component exhibits an omni-directional appearance as a result of the factor $(1–M^s \cos\theta)^6$ in the numerator of equation (21). The shift in the spectral peak with angle is primarily due to the mean flow effects and is captured by the GF. Figure 7(a) shows similar comparisons in a Mach 0.98 jet. The agreement is generally good, both in level as well as the spectral peak location. Near the dominant radiation angle of the Mach 0.98 jet, however, differences start to emerge. The data point to a distinct spectral peak near the 150° inlet angle and at the Strouhal number of 0.20. It is suggested here that this peak may be influenced by the Kelvin-Helmhotz instabilities, which manifest themselves at high subsonic and supersonic Mach numbers. These waves dominate the distinct directivity of high-speed jet noise at shallow angles, and their peak radiation frequency is sometimes scaled with Helmholtz number ($He \equiv f D_J/c_\infty$).

Similar comparisons are also shown in figure 7(b) for the five supersonic jets. The presence of shock noise in the spectra is quite visible. These predictions exhibit increasing deterioration at shallow angles. The 150° spectra peak at a lower frequency relative to measurements and show a deficit in noise level. It is conceivable that, in addition to the instability-related noise, jet spread could also play a role at high speeds and near the zone of *relative* silence. A parallel flow model tends to exaggerate the High Frequency (HF) refraction (refs. 21 to 23). The actual decay rate into the zone of silence is relatively less steep when the HF-GF is calculated in a spreading jet. The effect of jet spread on Low Frequency (LF) noise is less clear and yet to be examined. For long waves, the *locally parallel flow* assumption is more likely to deteriorate when the mean flow is not slowly varying on a wavelength scale. On the other hand, it is also argued that refraction is relatively weak at low frequency.

8. Hot Jets

When the acoustic Mach number exceeds the sonic point, the factor $(1-M^s \cos\theta)$ appearing in the denominator in the compressible Rayleigh equation becomes singular. The numerical integration should now continue along an appropriate path in the complex plane, and around the singularity (ref. 10). A better illustration of the GF that shows its scaling with respect to square root of density is defined in equation (35). The factor $(1-M^s \cos\theta)$ is also multiplied by the GF to demonstrate the transition into the zone of silence at $\cos\theta = 1/M^s$.

$$\Lambda(\vec{x},\vec{x}^s,\omega) \equiv (1-M^s\cos\theta)(\rho^s/\rho_\infty)^{-0.5} D(\vec{x},\vec{x}^s,\omega) \tag{35}$$

Factor D^2 was defined in equation (33). As noted above, the appearance of the density factor in equation (35) solely serves to show that the GF scales with the square root of density at moderate to high frequency. This is examined by observing the behavior of the GF at 90°.

Figures 8(a) and (b) show the GF for a stationary ring source in a Mach 0.90 hot jet, and at a temperature ratio of T_r = 2.78. At this temperature the acoustic Mach number is supersonic (i.e., $U/c_\infty = 1.45$). Inspection of the GF at $\theta = 90°$ and at $St = 0.10$ shows some dispersion with the source location (fig. 8(a)). Figure 8(b) shows that the above density scaling is successful at St = 1.0. More importantly, this figure demonstrates that in the mid- to high frequency range, the GF equation (14) scales like $(1-M^s \cos\theta)^{-1}$ outside its zone of silence

It is also evident that compared to unheated subsonic jets discussed earlier, the zone of silence has grown in size irrespective of the frequency (see figs. 3(a) and 8(a)). The implications are that the above GF is not going to provide the required noise directivity near the peak radiation angle. Figures 9(a) and (b) show similar results for a convecting ring source. Figure 10 compares the 90° spectrum in a Mach 0.801, T_r =3.0 hot jet as calculated with an exact GF as well as a density-scaled GF (i.e., GF is simply set equal to $\rho^{1/2}/\rho^{1/2}$). The difference is fairly small and limited to the low frequency range.

The spectrum at R/D_J = 100 at SP49 (table 2) is also compared with the SHJAR data as seen in figure 11. Consider the 90° spectrum, which exhibits a deficit of 3 to 8 dB relative to measurements. This spectrum is entirely defined through equation (21), which according to the preceding arguments scales the sound spectral density asρ^3, in addition to the usual $\kappa^{7/2}$ scaling. Therefore, the mean density reductions caused by heat addition need to be compensated for by other resources in order to reach the required noise level. The choices available are: (a) additional noise sources due to heat; (b) changes in turbulence and/or its scales; or some combination of (a) and (b).

Lighthill's formulation of the acoustic analogy shows that in the absence of the viscous stress tensor, the source consists of an additional term$(p'-c_{\infty}^{2}\rho')$. When entropy fluctuations are neglected, this becomes $(c^{2}-c_{\infty}^{2})\rho'$ which is not necessarily small compared to terms usually kept in the equation. Unfortunately ρ' now appears on both sides of the equation. Other forms of the analogy have tried, for example, new definitions for the dependent variable, in an effort to restrain the impact of those inconvenient terms that are usually neglected. It is argued (ref. 7) that the second term on the right hand side of equation (3) is of the order of $(U/c)^{2}(u^{2}/\ell)$ relative to the first term that scales like (u^{2}/ℓ). In the Mach 0.90 example seen in figure 11, the second term has a magnitude of 0.81 compared to the first, which makes it relatively significant. Modeling of this term, however, poses new difficulties due to the appearance of p' in the source.

In the latest formulation of the acoustic analogy, reference 24 selects a new dependent variable, referred to as the generalized pressure, and writes the third-order wave equation in a form that does not include the dependent variable as part of the source.

Tam et al. (ref. 25) modified their $k\varepsilon$ turbulence model in order to improve their fine-scale predictions for hot jets. They proposed a new addition to the turbulent viscosity, as related to the mean density gradient, which accounts for enhanced mixing and increased growth of the shear layer when jets are hot. More recently (ref. 26), they modified their two-point space-time correlation model to increase its decay rate for hot jets. This new model, which takes advantage of four additional empirical parameters, provides improved prediction for hot jets at mid-angles.

Shown in figures 12(a) through (c) are the predicted turbulent kinetic energy for the 2 in. convergent nozzle at set points SP03, SP07, and SP49 (see tables 1 and 2), using a modification to the baseline κ–ε model in the Wind code that incorporates variable diffusion coefficients (ref. 27) in the transport equations for κ and ε. The objective of this modification was to enable more accurate calculation of the jet potential core region, and in particular, the faster transport of turbulent kinetic energy to the jet centerline observed in experiments, which has not been captured well by standard κ–ε models. Using this modified κ–ε model, favorable agreement with the PIV measurements (ref. 16) are observed in the turbulence levels, as well as the shortening of the core length due to the heat–which is the product of a faster jet spread and improved mixing. Consequently, it is quite compelling to attribute the noise deficit observed in the predictions of figure 11 to heat-related sources, and/or changes in the turbulence scales, which in turn, may influence the decay rate of a two-point correlation.

Near the downstream jet axis, the instability-related noise quickly overwhelms the hot jet solution. The problem is also compounded due to a gradual deterioration in the parallel flow model at higher jet speeds and at small angles, as discussed in the latter part of section 7.

9. Assumptions and Future Work

This paper details some important features of the source and the propagation Green's function in a model-based jet noise prediction methodology. A number of hypotheses are made in calculating the far-field sound:

A careful examination of the propagation filter shows that in a locally parallel flow the zone of silence grows increasingly large with jet velocity. It could encompass a sizeable region near the downstream jet axis as the acoustic Mach number becomes supersonic. A parallel flow model is known to increasingly exaggerate the high frequency refraction at higher jet speeds (refs. 21 and 23). When the GF is calculated in a truly spreading jet, the actual decay rate into the cone of *relative* silence is less steep. Low frequency noise may also be influenced by the jet spread–although the effect is less clear and needs to be determined. In general, a parallel flow model is expected to provide reliable *sideline* predictions, and to become effective in a broader angle range at lower jet speeds.

TABLE 3.—LIST OF JENO ASSUMPTIONS

	Assumption	Reference
1	Turbulence is assumed as quasi-normal in order to reduce the order of the fourth order correlations	eq. 22(a)
2	Fluid viscosity and heat conduction are not considered to be important in sound generation.	eq. 1
3	Turbulence is considered as isotropic	eq. F1; also ref. 14
4	Exponential spatial and temporal functions are utilized to model a two-point correlation function	eq. 23
5	A non-compact source is considered	eq. 27
6	The non-causal GF is calculated for a locally parallel flow	eq. 1
7	The second component of the GF, believed to be associated with the instability waves, is not addressed	see ref. 3
8	The heat-related sources were not modeled	see equation after eq. 4
9	Two constants are utilized in connection with the time-and length scales. Third constant relates turbulent kinetic energy conversion to sound. Fourth constant removes singular behavior of the Doppler factor.	eq. 24 eq. 30 eq. B6

The second component of the Green's function (i.e., the causal GF) is instability related, and dominates the spectrum at shallow angles to the jet axis. This component needs to be addressed as a high priority in supersonic jets. Some preliminary results calculated for a simplified source in a model jet (ref. 3) show encouraging qualitative agreement with data.

It was also shown that a non-compact source model predicts a proper high-frequency roll-off. As the wavelength of the sound generated within a turbulent eddy becomes shorter than the correlation length-scale, a phase cancellation is initiated that shapes the spectral roll-off at high frequency. It is not surprising that this fall-off should be sensitive to the spatial form of the correlation in relationship to the wavelength of the sound it generates. Various spatial functions such as Gaussian versus exponential become distinguishable from one another when the source is considered as non-compact.

Although the formulation and validation cases presented here are limited to unheated jets, we took the liberty to evaluate a sample hot case to demonstrate the shortfalls and possible solutions. The deficit in the predicted noise level was attributed to any number of the following:

- Calibration of the usual two-equation turbulence model.
- Possible additional sources such as enthalpy fluctuations.
- Decay of a two-point space-time correlation as affected by heat.
- The effect of heat on turbulence length- and time-scales.

Experimental studies are currently underway at the NASA Glenn Research Center to address items (c) and (d) above. In addition, turbulence model development work is ongoing in the Wind code with the addition of linear two-equation and explicit algebraic stress models specifically calibrated for jet flows. However, the favorable comparisons of PIV measurements with RANS calculations using a modified κ–ε model presented here indicate that the RANS input is not the sole source of disagreement between calculated and experimentally measured jet noise. It is hoped that these efforts may shed light on this somewhat elusive relationship between the turbulence in hot jets and its far-field noise.

To reiterate, version 1.0 of JeNo is applicable to cold, round jets of subsonic velocity. It correctly predicts sound for all angles at such conditions. It does not correctly predict hot jets, jets of strong asymmetry, or jets with supersonic (relative to ambient speed of sound) exit velocities.

10. Appendix A.—Numerical Solution to Compressible Rayleigh Equation

In a cylindrical coordinate system, the second order compressible Rayleigh operator governing function f_m is written as (ref. 10)

$$\begin{gathered} f_m'' + \left[\frac{1}{r} - \frac{\rho'}{\rho} - 4\cos\theta \frac{M'}{(1 - M\cos\theta)}\right] f_m' + \\ \left[\frac{\omega^2}{c^2}(1 - M\cos\theta)^2 - \frac{m^2}{r^2} - \frac{\omega^2}{c_\infty^2}\cos^2\theta + \frac{3\cos\theta}{(1 - M\cos\theta)}\left(\frac{\rho'}{\rho}M' - \frac{1}{r}M' - M''\right)\right] f_m = 0, \end{gathered} \tag{A1}$$

where prime denotes a radial derivative. Having specified the jet profiles $M = U(r)/c_\infty$ and $c^2 = \gamma \Re T(r)$, the numerical solution to (A1) starts with $f_m = a_m \mathrm{r}^m$ as $r \to 0$ and continues to the jet boundary at $r = R_o$ where the function and its derivative are matched with the appropriate outgoing solution outside the jet. Constant a_m thus becomes

$$\begin{gathered} a_m = (-i)^m \varepsilon_m \frac{k\sin\theta [J_m(\chi) H'^{(1)}_m(\chi) - J'_m(\chi) H^{(1)}_m(\chi)]}{k\sin\theta\, f_m(R_o) H'^{(1)}_m(\chi) - df_m(R_o)/dr\, H^{(1)}_m(\chi)} \\ \varepsilon_m = \begin{cases} 1, m = 0 \\ 2, m \geq 1 \end{cases} \end{gathered} \tag{A2}$$

In equation (A2), prime as appearing on the cylindrical Bessel and Hankel functions points to a derivative with respect to the argument $\chi = kR_o \sin\theta$.

11. Appendix B.—Doppler Factor Singularity

When a compact source is moving towards an observer at the speed of sound, equation (13) shows that the observer frequency $\omega \to \infty$ as $M_c \cos\theta \to 1$. We may introduce a non-compact source in equation (6) by allowing the axial source position to be a complex number, with a small imaginary part

$$x_1^s \to x_1^s(1+i\alpha M_c), \quad \alpha \to 0 \tag{B1}$$

Mathematically, real parameter α allows a slight perturbation in the vicinity of the actual source location x_1^s. Equation (11) is written as

$$\int_{y_1} e^{-iky_1(1+i\alpha M_c)\cos\theta} e^{-i(\omega^s-\omega)y_1/U_c} dy_1 = 2\pi\delta\{-\frac{\omega}{U_c}[1-M_c(1+i\alpha M_c)\cos\theta]+\frac{\omega^s}{U_c}\}, \quad \alpha \to 0 \tag{B2}$$

Note that when the factor multiplying y_1 in the exponent of the above integrand is not zero, small parameter α should be selected appropriately to let the integrand converge at large y_1

$$\begin{gathered}\int_{y_1} e^{\beta y_1} e^{-i(k\cos\theta+\frac{\omega^s-\omega}{U_c})y_1} dy_1 = \frac{\beta^- - \beta^+}{(\beta^+ - i\chi)(\beta^- - i\chi)}, \quad \begin{cases}\alpha = \alpha^+ \to 0^+, y_1 < 0 \\ \alpha = \alpha^- \to 0^-, y_1 > 0\end{cases} \\ and \quad \beta \equiv \alpha k M_c \cos\theta, \quad \chi \equiv k\cos\theta + \frac{\omega^s - \omega}{U_c}\end{gathered} \tag{B3}$$

Thus, the integral equation (B3) approaches zero as $a \to 0$, *(i.e.,*$\beta^+ \to \beta^-$). The delta function in equation (B2) is subsequently placed in equation (10). The integration with respect to ω requires

$$\omega^s = \omega[(1-M_c\cos\theta) - i\alpha M_c^2\cos\theta], \quad as\ \alpha \to 0. \tag{B4}$$

Since frequencies are real numbers, we may now define the modified Doppler factor as the magnitude of the above complex frequency

$$\omega^s = \omega[(1-M_c\cos\theta)^2 + (\alpha M_c)^2]^{1/2}, \quad as\ M_c\cos\theta \to 1 \tag{B5}$$

or

$$(1-M_c\cos\theta) \to [(1-M_c\cos\theta)^2 + \alpha^2 M_c^2]^{1/2} \tag{B6}$$

12. Appendix C.—Far-Field Spectral Density

The acoustic pressure fluctuation at the observer point $\vec{x}$ and time t resulting from source Q emitting at point $\vec{y}$ and time t_1 is

$$p(\vec{x},t) \quad \iint G(\vec{x},t;\vec{y},t_1)Q(\vec{y},t_1)dt_1 d\vec{y}, \tag{C1}$$

where

$$G(\vec{x},t;\vec{y},t_1) = \frac{1}{2\pi}\int_{-\infty}^{+\infty} G(\vec{x},\vec{y},\omega)e^{-i\omega(t-t_1)}d\omega\,, \tag{C2}$$

and $G(\vec{x},\vec{y},\omega)$ is an appropriate frequency-domain Green's function. The sound spectral density is a Fourier transform of the auto-correlation function

$$\overline{p^2}(\vec{x},\omega) = \int_{-\infty}^{+\infty} e^{i\omega\tau}d\tau \int_{-\infty}^{+\infty} p(\vec{x},t)p(\vec{x},t+\tau)dt. \tag{C3}$$

Upon placing equation (C1) in equation (C3) we find

$$\overline{p^2}(\vec{x},\omega) = \int_{-\infty}^{+\infty} e^{i\omega\tau}d\tau \int_{-\infty}^{+\infty} dt \left\{ \int_{t_1}\int_{\vec{y}_1} G(\vec{x},t;\vec{y}_1,t_1)Q(\vec{y}_1,t_1)dt_1 d\vec{y}_1 \right\} \left\{ \int_{t_2}\int_{\vec{y}_2} G(\vec{x},t+\tau;\vec{y}_2,t_2)Q(\vec{y}_2,t_2)dt_2 d\vec{y}_2 \right\}.$$

Equation (C2) is now placed in the preceding expression to obtain

$$\overline{p^2}(\vec{x},\omega) = (\frac{1}{2\pi})^2 \int_{-\infty}^{+\infty} e^{i\omega\tau}d\tau \int_{-\infty}^{+\infty} dt \left\{ \int_{\omega_1}\int_{t_1}\int_{\vec{y}_1} G(\vec{x},\vec{y}_1,\omega_1)e^{-i\omega_1(t-t_1)}Q(\vec{y}_1,t_1)d\omega_1 dt_1 d\vec{y}_1 \right\} \times$$
$$\left\{ \int_{\omega_2}\int_{t_2}\int_{\vec{y}_2} G(\vec{x},\vec{y}_2,\omega_2)e^{-i\omega_2(t+\tau-t_2)}Q(\vec{y}_2,t_2)d\omega_2 dt_2 d\vec{y}_2 \right\}. \tag{C4}$$

The integration with respect to t gives $2\pi\delta(\omega_1+\omega_2)$, which is followed by an integration with respect to ω_2, resulting in

$$\overline{p^2}(\vec{x},\omega) = \frac{1}{2\pi}\int_{-\infty}^{+\infty} e^{i\omega\tau}d\tau \int_{\omega_1}\int_{t_1}\int_{\vec{y}_1}\int_{t_2}\int_{\vec{y}_2} G(\vec{x},\vec{y}_1,\omega_1)G(\vec{x},\vec{y}_2,-\omega_1)Q(\vec{y}_1,t_1)Q(\vec{y}_2,t_2)e^{i\omega_1 t_1}$$
$$e^{i\ \ _1(\ \ t_2)}d\ \ _1 dt_1 dt_2 d\vec{y}_1 d\vec{y}_2.$$

The integration with respect to τ gives a delta function

$$\int_{-\infty}^{+\infty} e^{i(\omega+\omega_1)\tau}d\tau = 2\pi\delta(\omega+\omega_1).$$

Subsequent integration with respect to ω_1 results in

$$\overline{p^2}(\vec{x},\omega)=\int_{t_1}\int_{\vec{y}_1}\int_{t_2}\int_{\vec{y}_2} G(\vec{x},\vec{y}_1,-\omega)G(\vec{x},\vec{y}_2,\omega)Q(\vec{y}_1,t_1)Q(\vec{y}_2,t_2)e^{-i\omega(t_1-t_2)}dt_1dt_2d\vec{y}_1d\vec{y}_2. \tag{C5}$$

We now require that source function Q be a stationary function, i.e. $Q = 0$ when $|t|$ T, for some large time T. For a stationary source, the average value

$$\overline{|Q(\vec{y},t)|^2} - \frac{1}{2T}\lim_{T}\int_{T}^{T}|Q(\vec{y},t)|^2 dt \tag{C6}$$

remains finite. Let

$$q(\vec{y},\omega,T)=\frac{1}{2\pi}\int_{-T}^{+T}Q(\vec{y},t)e^{i\omega t}dt. \tag{C7}$$

We define a time-domain cross-correlation

$$R(\vec{y},\vec{\xi},\tau)\equiv\overline{Q^*(\vec{y}_1,t)Q(\vec{y}_2,t+\tau)}=\lim_{T\to\infty}\frac{1}{2T}\int_{-T}^{+T}Q^*(\vec{y}_1,t)Q(\vec{y}_2,t+\tau)dt, \tag{C8}$$

where $\vec{\xi}$ and τ denote the spatial and temporal separations between points $\vec{y}_1=\vec{y}-\vec{\xi}/2$, $\vec{y}_2=\vec{y}+\vec{\xi}/2$ and * indicates a complex conjugate. The Fourier transform of the cross-correlation function is given as

$$Q_{12}(\vec{y},\vec{\xi},\omega)=\int_{-\infty}^{+\infty}R(\vec{y},\vec{\xi},\tau)e^{i\omega\tau}d\tau, \tag{C9}$$

and is related to the spectral densities at points $\vec{y}_1$ and $\vec{y}_2$

$$\lim_{T\to\infty}\frac{1}{2T}q^*(\vec{y}_1,\omega,T)q(\vec{y}_2,\omega,T)=\frac{1}{(2\pi)^2}Q_{12}(\vec{y},\vec{\xi},\omega). \tag{C10}$$

Expression (C10) represents the spectral density for a two-point space-time correlation. Using the above equations in (C5) and noting that for a stationary process, the spectral intensity in now divided by $2T$ we find

$$\overline{p^2}(\vec{x},\omega)=\frac{(2\pi)^2}{2T}\int_{\vec{y}_1}\int_{\vec{y}_2}G(\vec{x},\vec{y}_1,-\omega)G(\vec{x},\vec{y}_2,\omega)q^*(\vec{y}_1,\omega,T)q(\vec{y}_2,\omega,T)d\vec{y}_1d\vec{y}_2, \tag{C11}$$

or

$$\overline{p^2}(\vec{x},\omega)=\int_{\vec{y}}\int_{\vec{\xi}}G^*(\vec{x},\vec{y}-\vec{\xi}/2,\omega)G(\vec{x},\vec{y}+\vec{\xi}/2,\omega)Q_{12}(\vec{y},\vec{\xi},\omega)d\vec{\xi}d\vec{y}. \tag{C12}$$

Upon using equation (C9) in equation (C12), the spectral density per unit volume of turbulence at $\vec{y}$ is given as in equation (15).

13. Appendix D.—Hase Variation of the Green's Function

The phase factor of a high-frequency Green's function for a convecting source, in the notation of reference 5 is

$$\exp\{ik[R+\frac{n}{k}(\varphi-\varphi^s)+\varsigma_n(r)-R\sin^2\theta]\}\,, \tag{D1}$$

where R denotes a source to observer distance, which in the present notation should be replaced with $(\vec{x}-\vec{y})$, and

$$\varsigma_n(r)=\int_{r_\delta}^{r} Q_n(r)dr\,, \tag{D2}$$

and r_δ is the zero crossing of the shielding function $Q_n(r)$,

$$Q_n^2(r)=(\frac{1-M\cos\theta}{c/c_\infty})^2-\cos^2\theta-(\frac{n}{rk})^2, \qquad Q_n(r_\delta)=0 \tag{D3}$$

The phase variation of the GF between source points $\vec{y}_1$ and $\vec{y}_2$ becomes

$$\exp\{ik[\Delta\xi_1\cos\theta+\frac{n}{k}\Delta\varphi^s+\Delta\varsigma_n(r^s)]\}\,, \tag{D4}$$

and

$$\Delta\varsigma_n(r^s)=\int_{r_1^s}^{r_2^s} Q_n(r)dr=\Delta r^s\sin\theta+\int_{r_1^s}^{r_2^s}\psi_n(r,\theta)dr \tag{D5}$$

The second term on the right hand side of (D5) signifies the effect of the refraction on phase. To the first order of approximation, this term may be neglected compared to the first term, which reflects the variations in phase due to source location only. As $k\rightarrow\infty$, equation (D4) becomes

$$\exp\{ik[\Delta\xi_1\cos\theta+\Delta r^s\sin\theta]\}\,, \tag{D6}$$

which is recognized as $\exp(i\vec{k}.\vec{\xi})$.

14. Appendix E.—Space-Time Correlation Models

When confronted with selecting the functional forms of the space-time correlation of velocity in a jet, several forms can be considered. Historically, these have been chosen partly based upon mathematical convenience, partly on data, and partly on compatibility with equations of motion. On the mathematical convenience, a model which has independent functions of space and time (in a moving frame) has often been chosen. And among functional forms for these independent functions, the Gaussian function has often been utilized for its ease of use in subsequent integrals. The Gaussian form also has the property of a zero derivative at the origin, making its Fourier transform integrable.

Measurements made with hot-wire probes, shown here from reference 17, and supported by PIV measurements (ref. 16), show that a Gaussian function is not particularly well-suited for describing the form of the space-time correlation near the origin. These data were acquired in a Mach = 0.50 cold jet flow, and show the behavior of the correlation function in the axial and radial separations. Figures E1 and E2 show the correlation of the axial and radial components, respectively, of velocity at three different locations in the jet: $x/D_J = 4$, $r/D_J = 0.50$ (lipline); $x/D_J = 8$, $r/D_J = 0.50$; and $x/D_J = 20$, $r/D_J = 1.25$. In each figure, the upper set of carpet plots show the correlation as a function of time delay and axial separation, while the lower plots show the correlation as a function of time delay and radial separation. There are interesting subtle variations in the correlations at the three locations in the jet, but they all show a very strong peaked behavior near the origin. Future versions may benefit from turbulence models which pick up the more subtle behaviors of these correlation functions, but at this time single-exponent models, such as equation 23, are better supported by data than Gaussian forms.

15. Appendix F.—Non-Compactness Factor

When wavelength of the acoustic disturbances is small relative to the correlation length scale (i.e., $\lambda < \ell$), it is shown (ref. 1) that the axial correlation coefficient I_{1111} (defined in eq. 25) consists of a non-compactness factor $N(k\ell)$ at high frequency. For example, using an exponential spatial function (see eq. 23) in the two-point correlation function of Batchelor, the axial correlation component R_{11} becomes

$$R_{ij}(\vec{\xi}) = \overline{u_1^2}[(f + \frac{1}{2}\xi f')\delta_{ij} - \frac{1}{2} f' \xi_i \xi_j / \xi], \tag{F1}$$

$$\xi = (\xi_1^2 + \xi_2^2 + \xi_3^2)^{1/2}, \qquad f(\xi) = e^{-\pi\xi/\ell} \tag{F2}$$

Note that for brevity, ξ is used here as the separation vector in a moving frame. Using (F2) in (F1) results in

$$R_{11}(\vec{\xi}) = \overline{u_1^2}[1 - \frac{\pi}{2\xi\ell}(\xi_2^2 + \xi_3^2)]e^{-\pi\xi/\ell} \tag{F3}$$

Upon placing (D3) into equation (25) we find

$$I_{1111}(\vec{y}, \omega^s) = 2H(\omega^s)\int_{\vec{\xi}} R_{11}^2(\vec{\xi}) e^{-i\vec{k}.\vec{\xi}} d\vec{\xi} \tag{F4}$$

The above integration my be performed in a spherical coordinate system $\vec{\xi} = (\xi\cos\alpha, \xi\sin\alpha\cos\phi, \xi\sin\alpha\sin\phi)$ and by selecting dummy variable $\vec{\xi}$ such that ξ_1 aligns with direction of radiation $\vec{k}$

$$I_{1111} = 2(\overline{u_1^2})^2 \ell^3 H(\omega^s) \int_{\xi=0}^{\infty} \int_{\phi=0}^{2\pi} \int_{\alpha=0}^{\pi} (1 - \frac{\pi}{2}\xi\sin^2\alpha)^2 \exp(-2\pi\xi - i\ell k\xi\cos\alpha)(\xi^2 \sin\alpha \, d\alpha d\phi d\xi) \tag{F5}$$

This leads to equation (27) with the non-compactness factor given as

$$N(k\ell) = 20(\frac{\pi}{k\ell})^5[3\tan^{-1}(\frac{k\ell}{2\pi}) - 2\frac{k\ell}{\pi}\frac{5(\frac{k\ell}{\pi})^2 + 12}{\left((\frac{k\ell}{\pi})^2 + 4\right)^2}], \quad \text{for} \quad f(\xi) = e^{-\pi\xi/\ell} \tag{F6}$$

The non-compactness factor thus becomes a function of the spatial form of the correlation. For example, when a Gaussian function $f(\xi) = \exp(-\pi\xi^2/\ell^2)$ is placed in (F1), equation (27) should be calculated from

$$N(k\ell) = \exp(-\frac{k^2\ell^2}{8\pi}), \quad \text{for} \quad f(\xi) = e^{-\pi\xi^2/\ell^2} \tag{F7}$$

16. References

1. Khavaran, J. Bridges, A parametric study of fine-scale turbulence mixing noise, Journal of Sound and Vibration, 279 (2005) 1131–1154.
2. C.K.W. Tam, L. Auriault, Jet mixing noise from fine-scale turbulence, AIAA Journal, 37 (1999) 145–153.
3. M.E. Goldstein, L.M. Handler, The role of instability waves in predicting jet noise, AIAA Paper 2003–3256, 2003.
4. D.C. Pridmore-Brown, Sound propagation in a fluid flowing through an attenuating duct, Journal of Fluid Mechanics, 4 (1958) 393–406.
5. D.W. Wundrow, A. Khavaran, On the applicability of high-frequency approximation to Lilley's equation, Journal of Sound and Vibration, 272 (2004) 793–830.
6. G.M. Lilley, On the noise from jets, noise mechanisms, AGARD-CP-131, (1974) 13.1–13.12.
7. M.E. Goldstein, An exact from of Lilley's equation with a velocity quadrupole/temperature dipole source term, Journal of Fluid Mechanics, 443 (2001) 232–236.
8. M.E. Goldstein, Aeroacoustics of turbulent shear flows, Ann. Rev. Fluid Mechanics, 16 (1984) 262–295.
9. T. Colonius, S.K. Lele, P. Moin, Sound generation in a mixing layer, Journal of Fluid Mechanics, 330 (1997) 375–409.
10. C.K.W. Tam, L. Auriault, Mean flow refraction effects on sound radiated from localized source in jets, Journal of Fluid Mechanics, 370 (1998) 149–174.
11. Agarwal, P.J. Morris, R. Mani, Calculation of sound propagation in nonlinear flows: suppression of instability waves, AIAA Journal, 42 (2004) 80–88.
12. M.E. Goldstein, S.J. Leib, Emission of sound from turbulence convected by a parallel mean flow in the presence of a confining duct, Journal of Sound and Vibration, 235 (2000) 25–42.
13. A.S. Monin, A.M. Yaglom, Statistical Fluid Mechanics: Mechanics of Turbulence, vol. 2 MIT Press, 1975.
14. G.K. Batchelor, The Theory of Homogeneous Turbulence, Cambridge University Press, Cambridge, 1960.
15. J. Bridges, M.P. Wernet, Turbulence measurements of separate flow nozzles with mixing enhancement features, AIAA Paper 2002–2484, 2002.
16. J. Bridges, M.P. Wernet, Measurements of the aeroacoustic sound source in hot jets, AIAA Paper 2003–3130, 2003.
17. J. Bridges, G.G. Podboy, Measurements of two-point velocity correlations in a round jet with application to jet noise, AIAA Paper 1999–1966, 1999.
18. P.O.A.L. Davies, M.J. Fisher, M.J. Barratt, The characteristics of turbulence in the mixing region of a round jet, Journal of Fluid Mechanics, 15, pt. 3, (1963) 337–367.
19. C.A. Hunter, R.H. Thomas, Development of a jet noise prediction method for installed jet configurations, AIAA Paper 2003–3169, 2003.
20. C.C. Nelson, G.D. Power, CHSSI Project CFD-7: The NPARC Alliance Flow Simulation System, AIAA Paper 2001–0594, January 2001.
21. Khavaran, E.A. Krejsa, Propagation of high frequency jet noise using geometric acoustics, AIAA Paper 93–0147, 1993.
22. Khavaran, Refraction and shielding of noise in non-axisymmetric jets, AIAA Paper 96–1780, 1996.
23. P.A. Durbin, High frequency Green's function for aerodynamic noise in moving media, part II: noise from a spreading jet," J. Sound and Vibration, 91(4), 1983, 527–538.
24. M.E. Goldstein, A generalized acoustic analogy, Journal of Fluid Mechanics, 488 (2003) 315–333.
25. C.K.W. Tam, A. Ganesan, A modified k-e turbulence model for calculating the mean flow and noise of hot jets, AIAA Journal, 42 (2004) 26–34.

26. C.K.W. Tam, N.N. Pastouchenko, K. Viswanathan, Fine scale turbulence noise from hot jets, AIAA Paper 2004–0362, 2004.
27. W.A. Engblom, N.J. Georgiadis, Investigation of variable-diffusion turbulence model correction for round jets, AIAA Paper 2005–3085, May 2005.
28. J. Bridges, G.G. Podboy, Measurements of two-point velocity correlations in a round jet with application to jet noise, AIAA Paper 1999–1966, 1999.

17. Figures

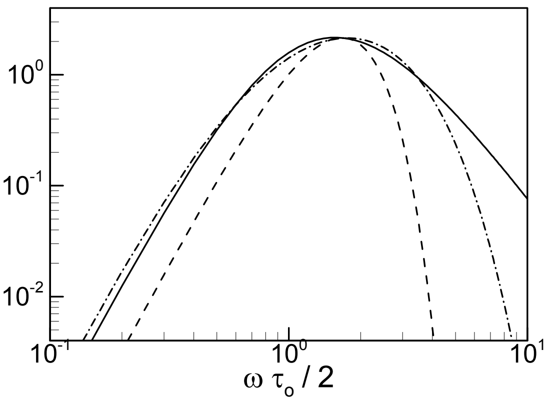

Figure 1.—Spectral shape function at 90° with temporal function defined as: $\exp(-|\tau/\tau_o|)$, solid line; $\exp\{-(0.4^2+\tau^2/\tau_o^2)^{0.50}\}$, dash-dot; $\exp(-\tau^2/\tau_o^2)$, dashed line.

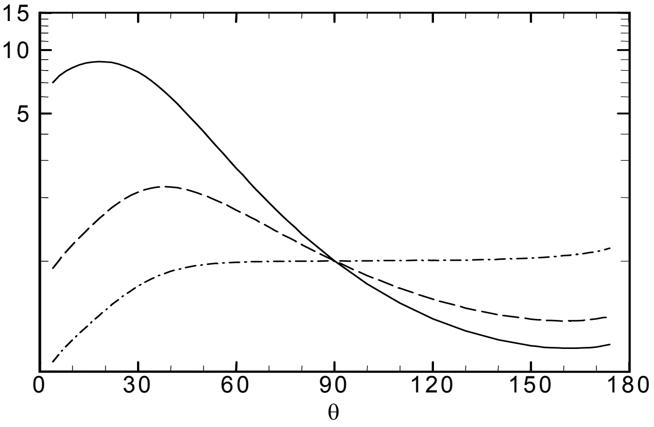

Figure 2(a).—Directivity $D(\vec{x},\vec{x}^s,\omega)$ due to a stationary ring source in a Mach 0.9 unheated jet at *St* = 0.10, x_1^s/D_J = 1.0 and r^S/D_J: 0.0 (solid line); 0.50 (dashed line); 1.0 (dash-dot).

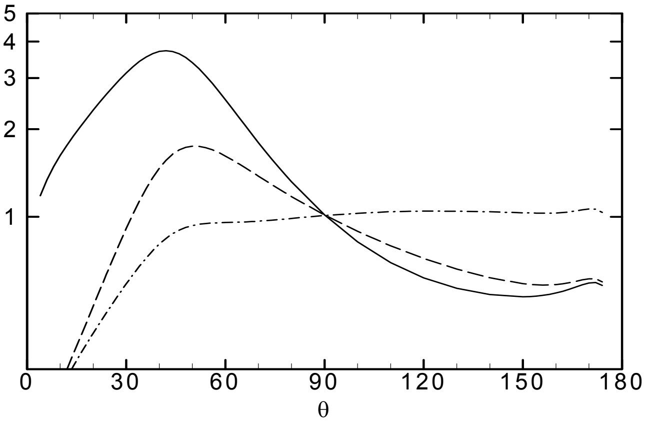

Figure 2(b).—As figure 2(a) but for *St* = 0.25.

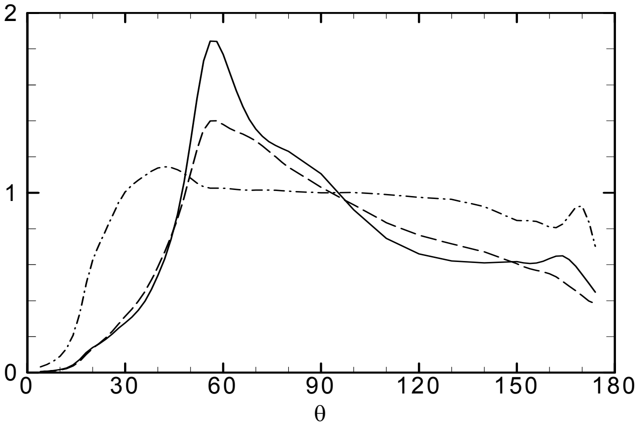

Figure 2(c).—As figure 2(a) but for *St* = 1.0.

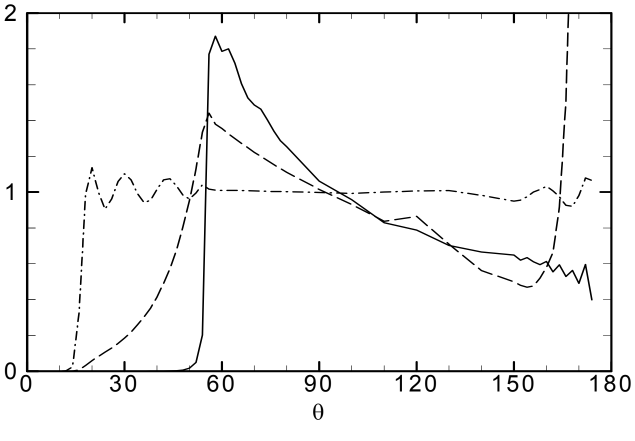

Figure 2(d).—As figure 2(a) but for *St* = 5.0.

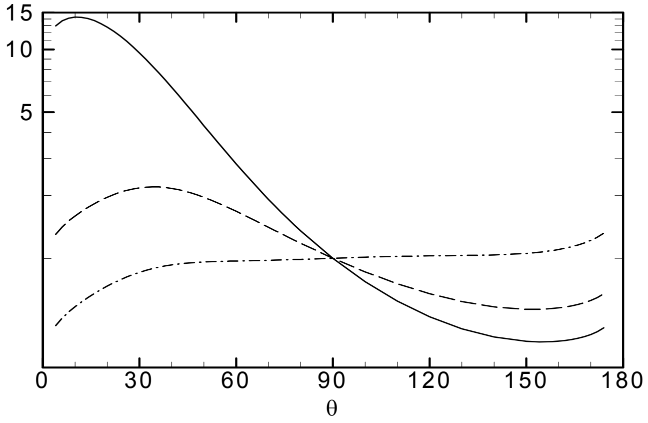

Figure 3(a).—Directivity $D(\vec{x},\vec{x}^s,\omega)$ due to a stationary ring source in a Mach 0.9 unheated jet at *St* = 0.10, $x_1^s/D_J = 7.5$ and r^s/D_J: 0.0 (solid line); 0.50 (dashed line); 2.0 (dash-dot).

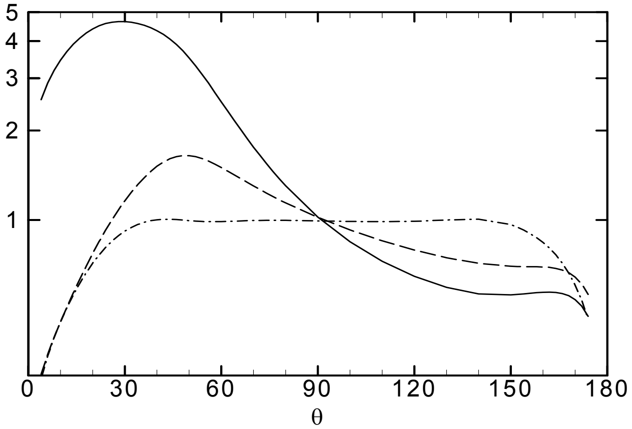

Figure 3(b).—As figure 3(a) but for *St* = 0.25.

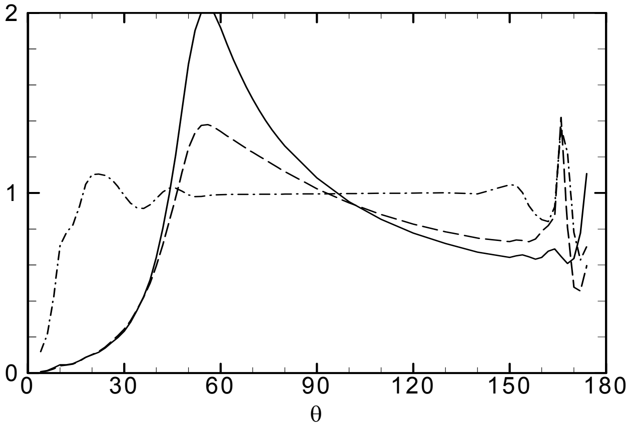

Figure 3(c).—As figure 3(a) but for *St* = 1.0.

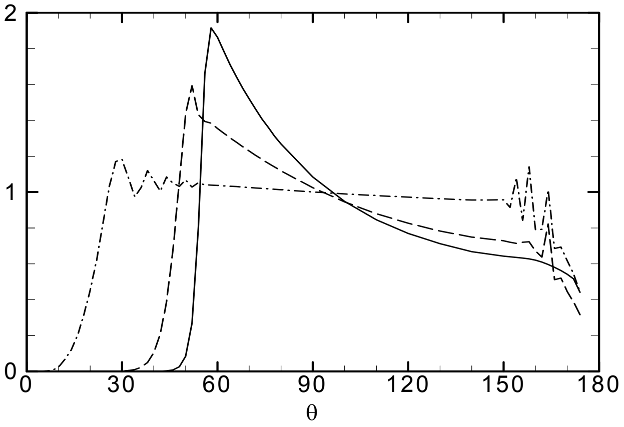

Figure 3(d).—As figure 3(a) but for *St* = 5.0.

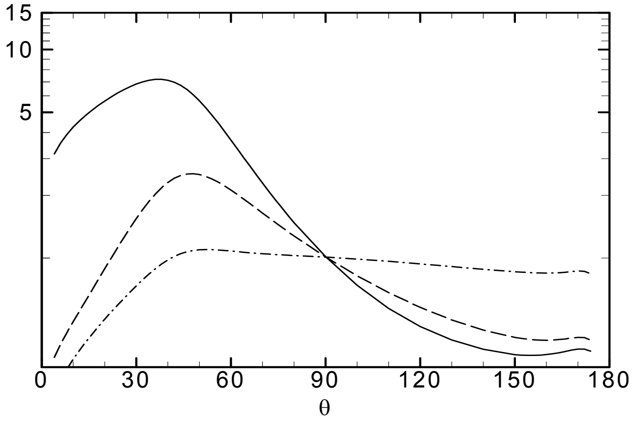

Figure 4.—Directivity $D(\vec{x},\vec{x}^s,\omega)$ due to a convecting ring source in a Mach 0.9 unheated jet at observer *St* = 0.25, x_1^s/D_J=1.0 and r^s/D_J: 0.0 (solid line); 0.50 (dashed line); 1.0 (dash-dot).

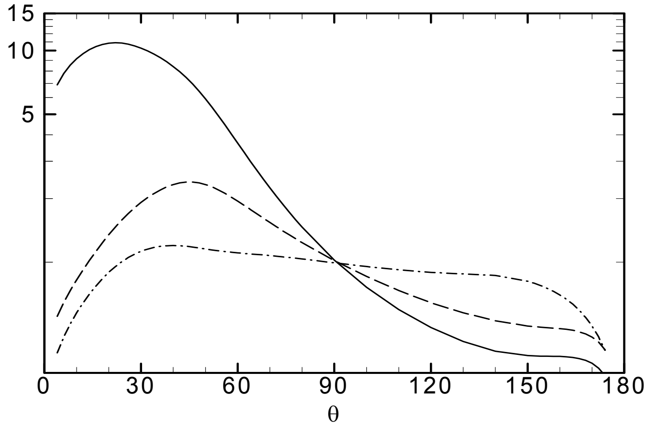

Figure 5.—As figure 4 but for a ring source at x_1^s/D_J=7.5 and r^s/D_J: 0.0 (solid line); 0.50 (dashed line); 2.0 (dash-dot).

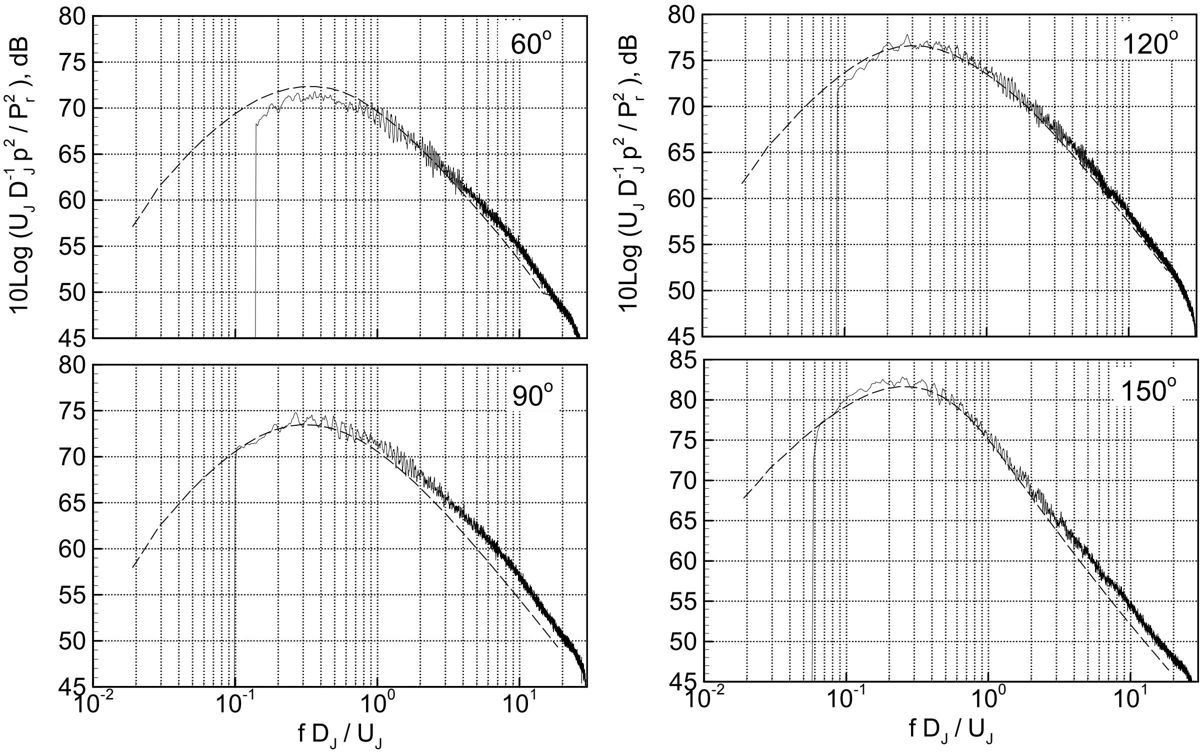

Figure 6.—Spectra in Mach 0.51, T_r =1.0 (SP03) jet at indicated inlet angles and at R/D_J = 100.

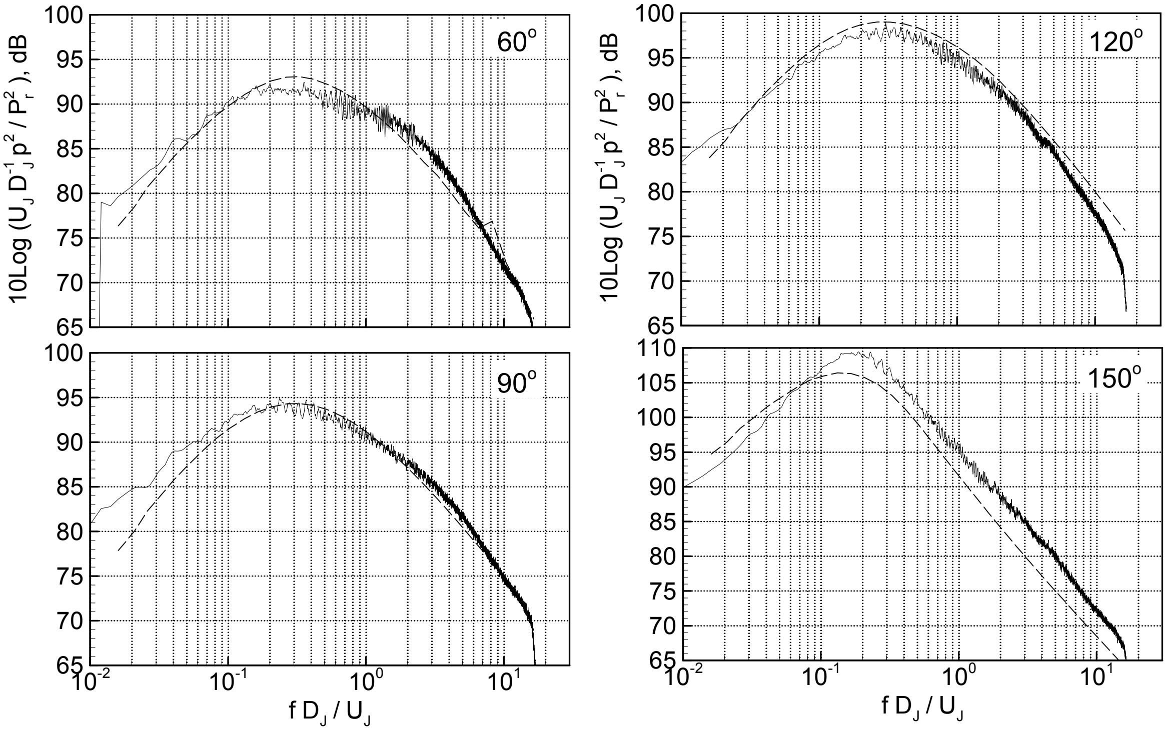

Figure 7(a).—Spectra in Mach 0.98, T_r =1.0 (SP07) jet at indicated inlet angles and at R/D_J = 100.

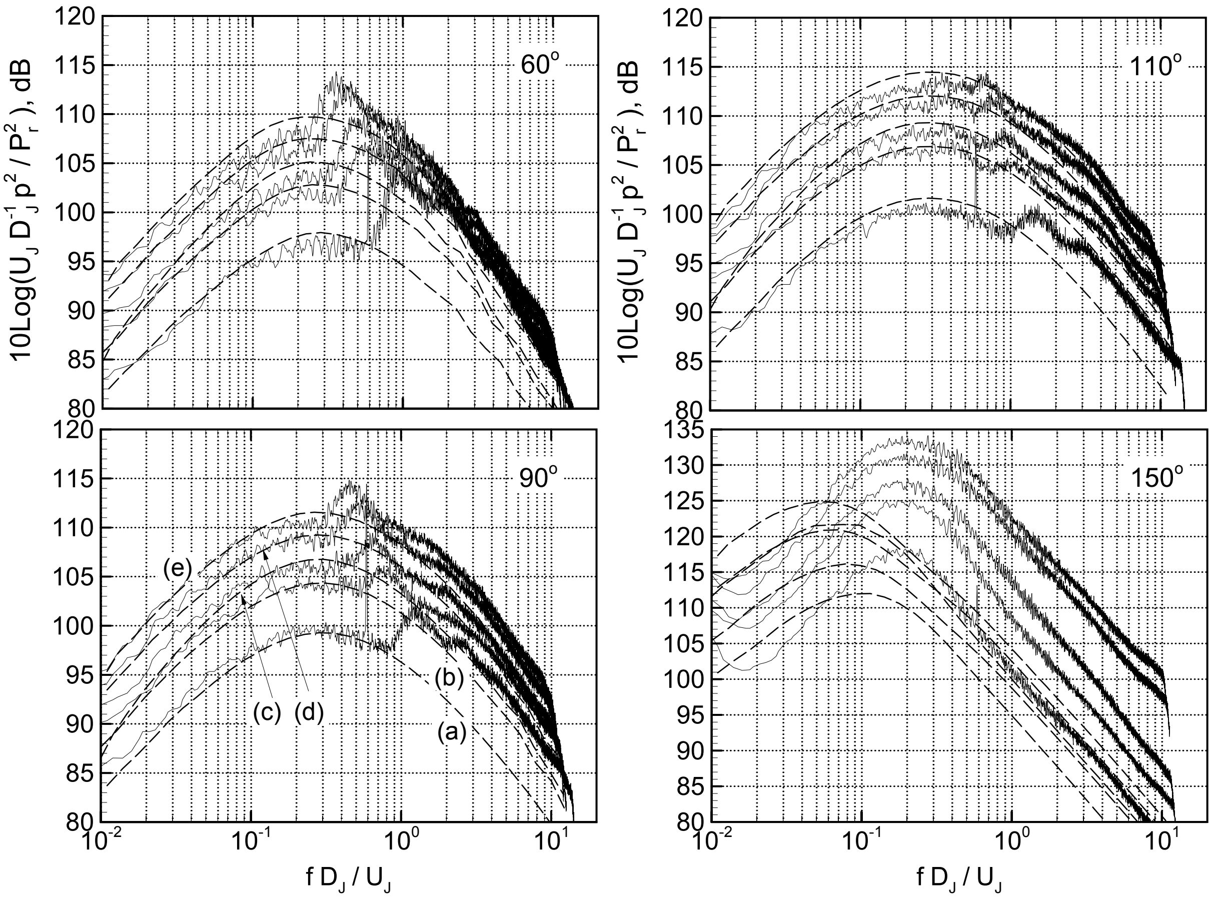

Figure 7(b).—Comparison between calculated spectra and data at indicated inlet angles at $r/D_J = 100$. (a) M_J =1.185, (b) M_J =1.40, (c) M_J =1.50, (d) M_J = 1.66, (e) M_J = 1.80.

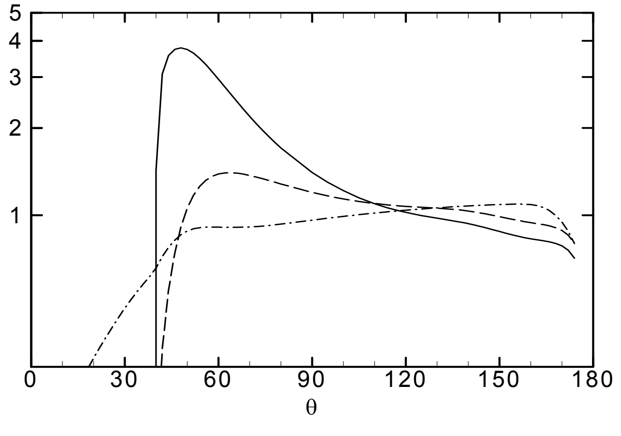

Figure 8(a).—Directivity $\Lambda(\vec{x},\vec{x}^s,\omega)$ due to a stationary ring source in Mach 0.9, T_r=2.78 jet at St = 0.10, x_1^s/D_J=7.5 and r^s/D_J: 0.0 (solid line); 0.50 (dashed line); 2.0 (dash-dot).

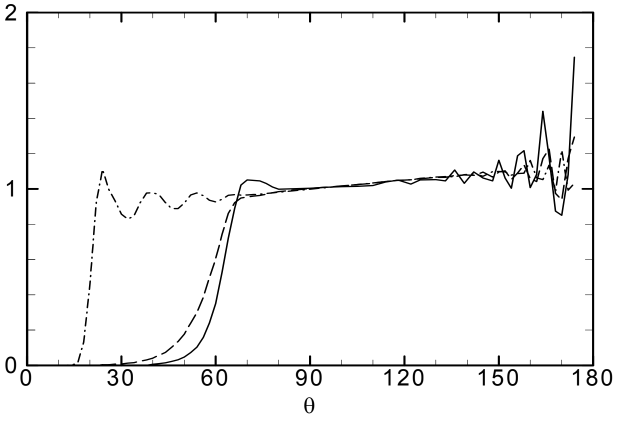

Figure 8(b).—As figure 8(a) but for a stationary ring source at *St* = 1.0.

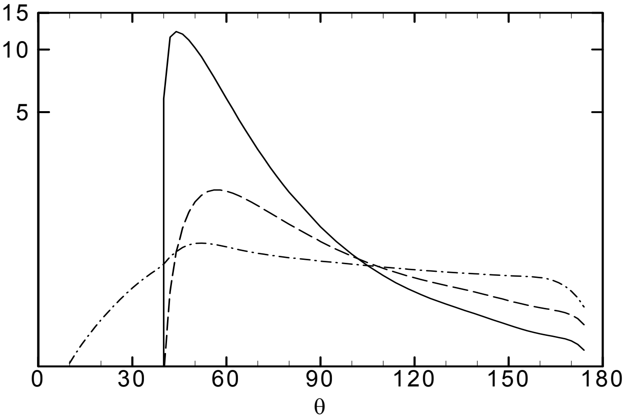

Figure 9(a).—As figure 8(a) but for a convecting ring source at observer St = 0.10.

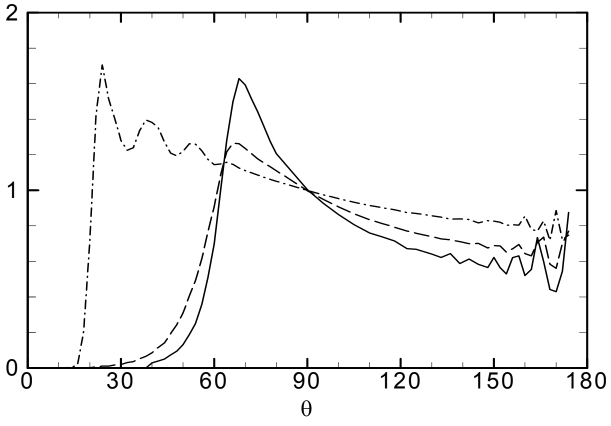

Figure 9(b).—As figure 8(a) but for a convecting ring source at observer *St* = 1.0.

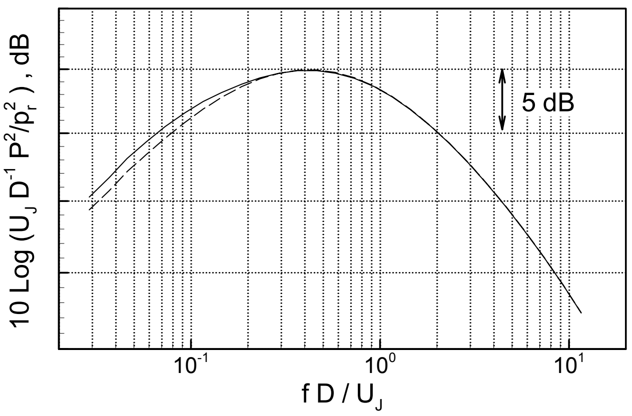

Figure 10.—Far-field spectrum at 90° in a Mach 0.801, T_r =3.0 jet. Exact Green's function (solid line); density-scaled GF (dashed line).

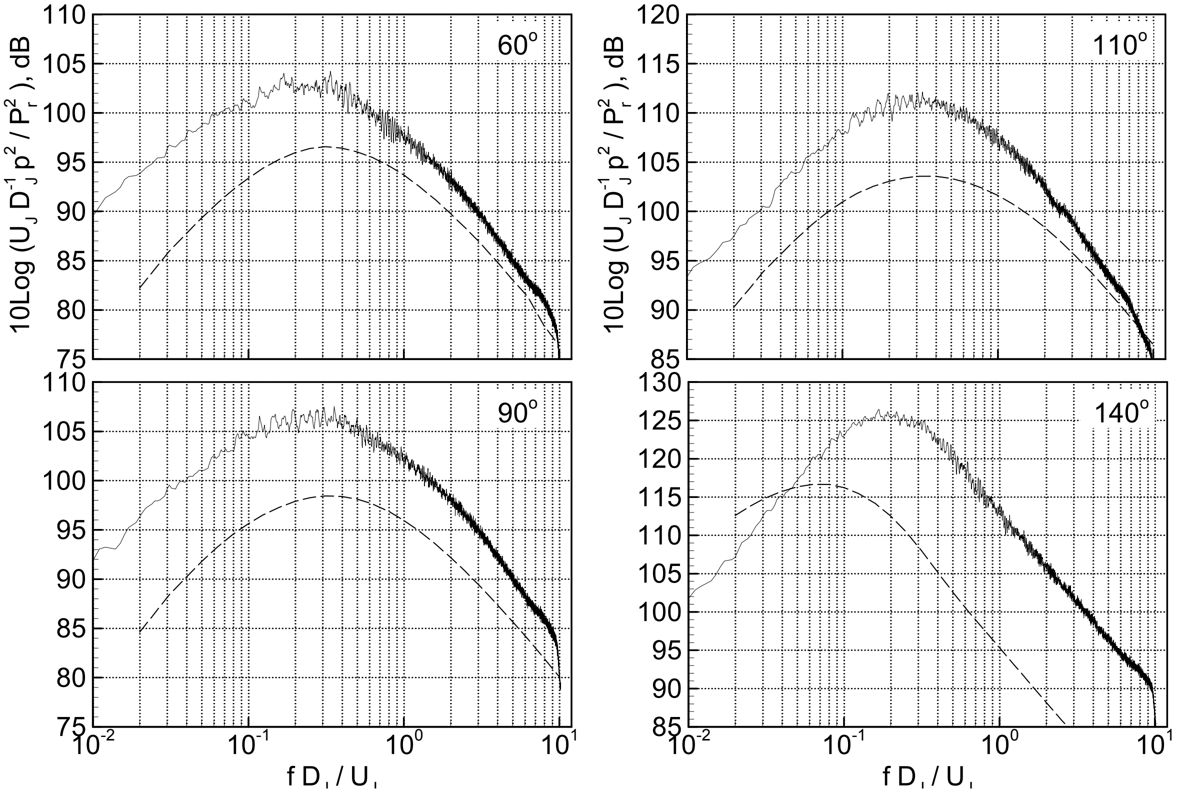

Figure 11.—Spectra in Mach 0.90, T_r =3.14 (SP49) jet at indicated inlet angles and at R/D_J = 100.

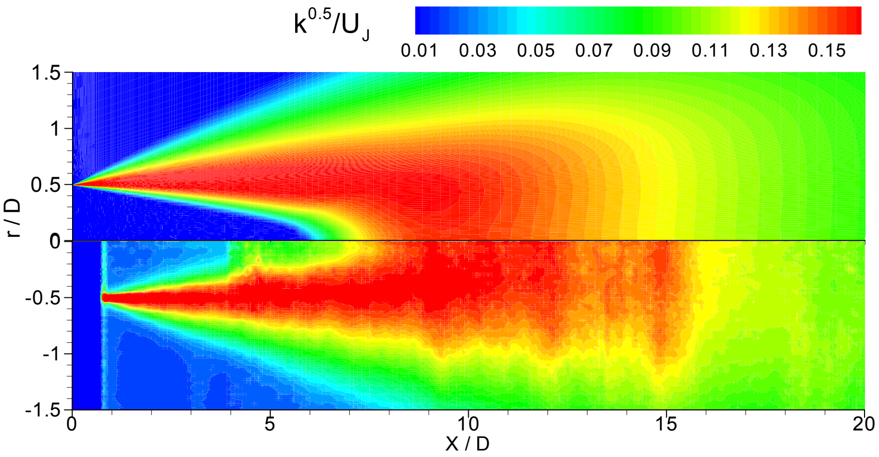

Figure 12(a).—Distribution of turbulent kinetic energy (SP03). Top half, RANS prediction; bottom half, PIV measurements.

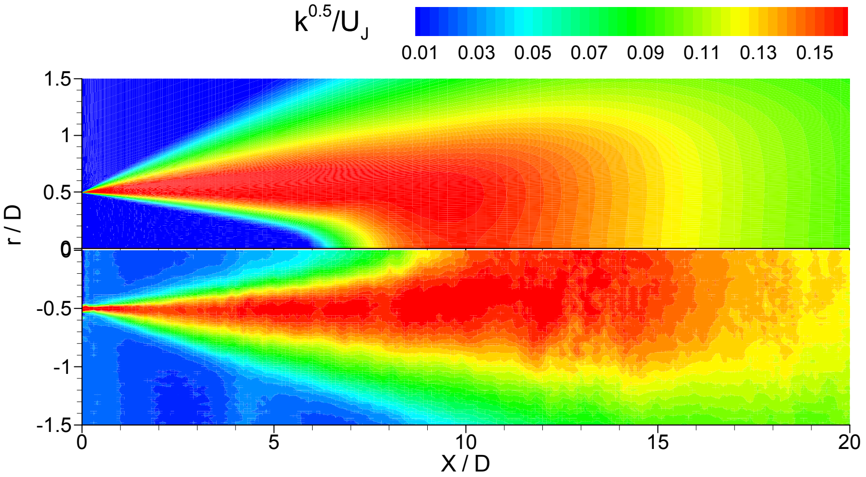

Figure 12(b).—Distribution of turbulent kinetic energy (SP07). Top half, RANS prediction; bottom half, PIV measurements.

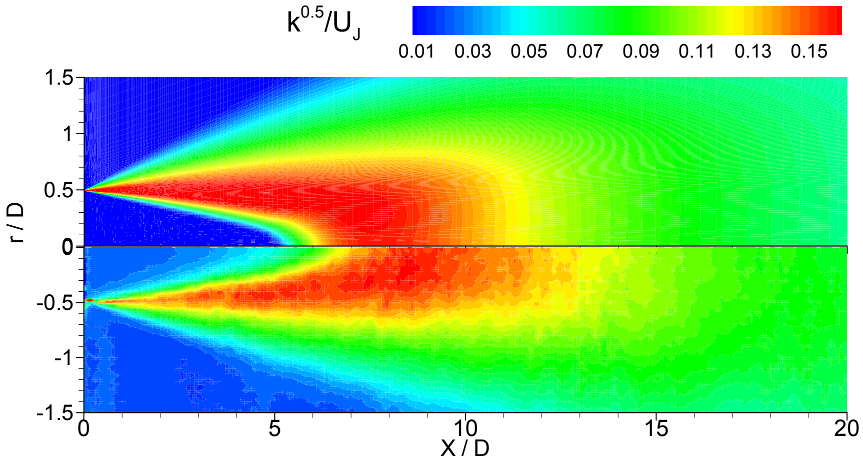

Figure 12(c).—Distribution of turbulent kinetic energy (SP49). Top half, RANS prediction; bottom half, PIV measurements.

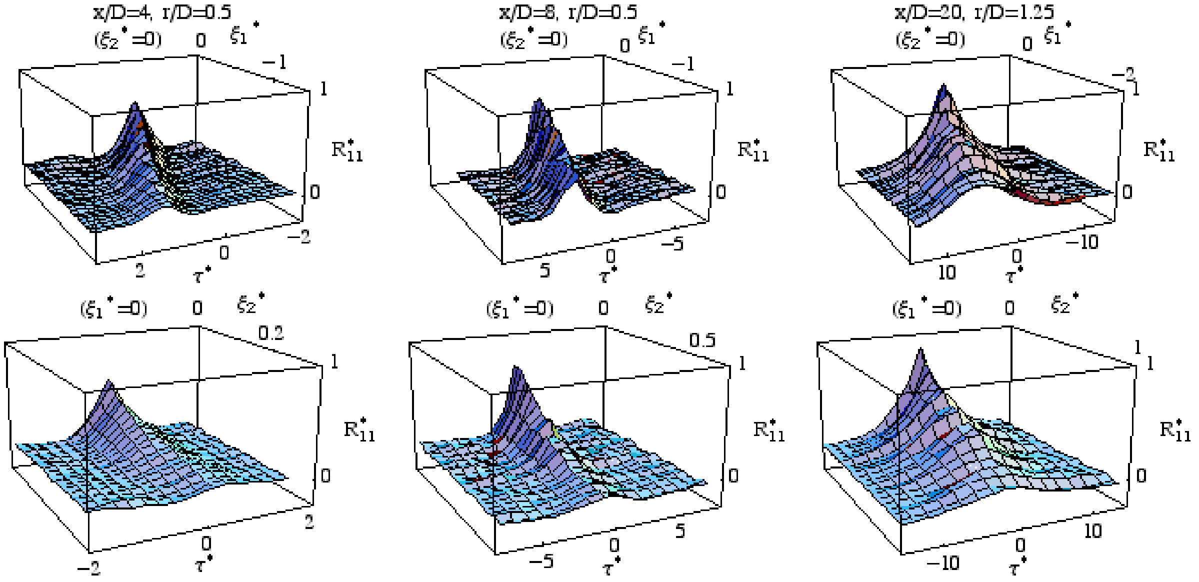

Figure E1.—Space-time correlation of $\overline{u_1 u_1'}$.

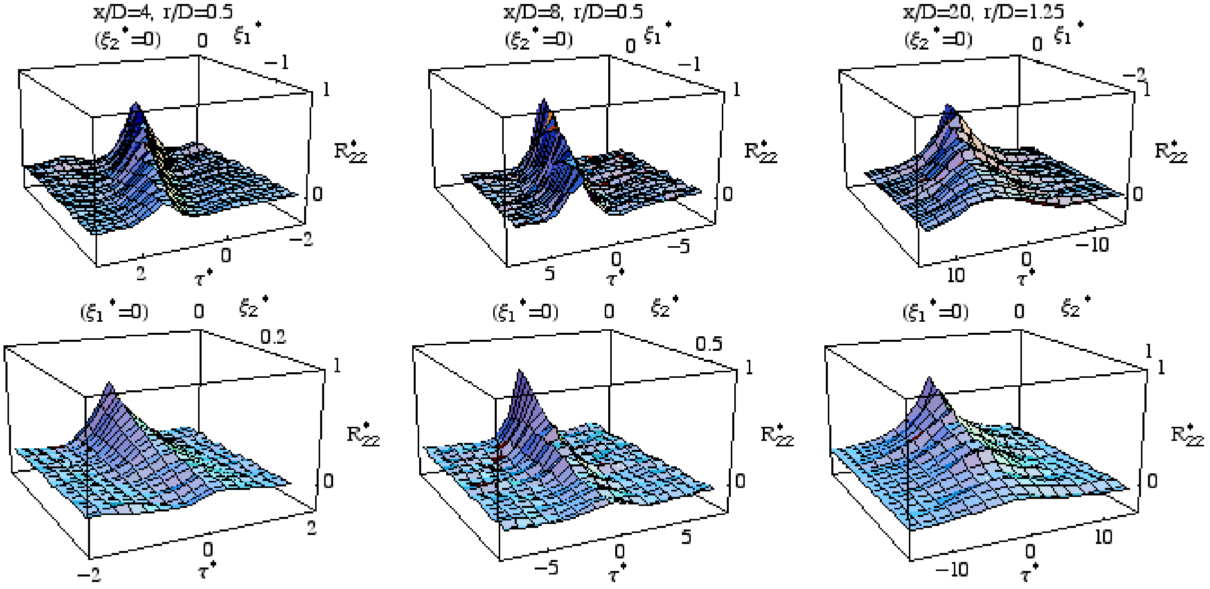

Figure E2.—Space-time correlation of $\overline{u_2 u_2'}$.

A comparison of the measurements with model forms using Gaussian and exponential functions is shown in reference 28.

REPORT DOCUMENTATION PAGE

Form Approved
OMB No. 0704-0188

Public reporting burden for this collection of information is estimated to average 1 hour per response, including the time for reviewing instructions, searching existing data sources, gathering and maintaining the data needed, and completing and reviewing the collection of information. Send comments regarding this burden estimate or any other aspect of this collection of information, including suggestions for reducing this burden, to Washington Headquarters Services, Directorate for Information Operations and Reports, 1215 Jefferson Davis Highway, Suite 1204, Arlington, VA 22202-4302, and to the Office of Management and Budget, Paperwork Reduction Project (0704-0188), Washington, DC 20503.

1. AGENCY USE ONLY (*Leave blank*)	**2. REPORT DATE** July 2005	**3. REPORT TYPE AND DATES COVERED** Technical Memorandum

4. TITLE AND SUBTITLE

Prediction of Turbulence-Generated Noise in Unheated Jets
Part 1: JeNo Technical Manual (Version 1.0)

5. FUNDING NUMBERS

WBS–22–781–30–70

6. AUTHOR(S)

Abbas Khavaran, James Bridges, and Nicholas Georgiadis

7. PERFORMING ORGANIZATION NAME(S) AND ADDRESS(ES)

National Aeronautics and Space Administration
John H. Glenn Research Center at Lewis Field
Cleveland, Ohio 44135 – 3191

8. PERFORMING ORGANIZATION REPORT NUMBER

E – 15186

9. SPONSORING/MONITORING AGENCY NAME(S) AND ADDRESS(ES)

National Aeronautics and Space Administration
Washington, DC 20546 – 0001

10. SPONSORING/MONITORING AGENCY REPORT NUMBER

NASA TM — 2005-213827

11. SUPPLEMENTARY NOTES

Abbas Khavaran, QSS Group, Inc., 21000 Brookpark Road, Cleveland, Ohio 44135; and James Bridges and Nicholas Georgiadis, NASA Glenn Research Center. Responsible person, Abbas Khavaran, organization code RTA, 216–977–1120.

12a. DISTRIBUTION/AVAILABILITY STATEMENT

Unclassified - Unlimited
Subject Categories: 02, 34, and 71

Available electronically at http://gltrs.grc.nasa.gov
This publication is available from the NASA Center for AeroSpace Information, 301–621–0390.

12b. DISTRIBUTION CODE

13. ABSTRACT ***(Maximum 200 words)***

The model-based approach, used by the JeNo code to predict jet noise spectral directivity, is described. A linearized form of Lilley's equation governs the non-causal Green's function of interest, with the non-linear terms on the right hand side identified as the source. A Reynolds-averaged Navier-Stokes (RANS) solution yields the required mean flow for the solution of the propagation Green's function in a locally parallel flow. The RANS solution also produces time- and length-scales needed to model the non-compact source, the turbulent velocity correlation tensor, with exponential temporal and spatial functions. It is shown that while an exact non-causal Green's function accurately predicts the observed shift in the location of the spectrum peak with angle as well as the angularity of sound at low to moderate Mach numbers, the polar directivity of radiated sound is not entirely captured by this Green's function at high subsonic and supersonic acoustic Mach numbers. Results presented for unheated jets in the Mach number range of 0.51 to 1.8 suggest that near the peak radiation angle of high-speed jets, a different source/Green's function convolution integral may be required in order to capture the peak observed directivity of jet noise. A sample Mach 0.90 heated jet is also discussed that highlights the requirements for a comprehensive jet noise prediction model.

14. SUBJECT TERMS Noise; Jet noise; Propulsion noise; Flow noise	**15. NUMBER OF PAGES** 41 **16. PRICE CODE**

17. SECURITY CLASSIFICATION OF REPORT Unclassified	**18. SECURITY CLASSIFICATION OF THIS PAGE** Unclassified	**19. SECURITY CLASSIFICATION OF ABSTRACT** Unclassified	**20. LIMITATION OF ABSTRACT**